Permeability Modeling of the Mars 2020 Parachute Broadcloth Material

Seyed Danial Ghasimi* and Jason Rabinovitch†
Stevens Institute of Technology, Hoboken, New Jersey 07030
Luis Chacon‡ and Savio J Poovathingal§
University of Kentucky Lexington, Lexington, Kentucky 40506
Cutler A Phillippe,¶ Collin Foster,** Laura Villafañe Roca,†† and Francesco Panerai‡‡
University of Illinois at Urbana-Champaign, Urbana, Illinois 61801
Faisal As'ad§§ and Charbel Farhat¶¶
Stanford University, Stanford, California 94305-3035
and
Marcus Lobbia*** and Navid Ataei†††
Jet Propulsion Laboratory, California Institute of Technology, Pasadena, California 91109

https://doi.org/10.2514/1.J065509

The broadcloth material used in parachute manufacturing is generally a thin, woven, permeable textile. The small length scales of fibers, pores, and gaps in fabric are challenging to spatially resolve in a full-scale parachute simulation. In this work, simulations are performed using a 3D reconstruction of the broadcloth material used in the Mars 2020 mission, and simulation results using the detailed reconstructed geometry are compared to a simplified model proposed in a previous work. Furthermore, results from simulations under Earth ambient lab conditions are compared to experimental permeability test data to validate the choice of parameters for this reduced-order model. Simulations under ASPIRE SR03 flight-relevant conditions are also performed to study permeability in a rarefied flow regime. It is observed that flow through the material is similar to a developing pipe flow, and under low-density conditions, significant slip velocity is present inside pores. For all conditions investigated, the pressure drag is the primary contributor to the total drag force. Drag and mass flow rate discrepancies are observed between models, motivating future work to investigate the sensitivity of system-level parachute FSI simulations to the assumed permeability model and associated parameters.

I. Introduction

SINCE the 1970s, NASA has used supersonic Disk-Gap-Band (DGB) parachutes to decelerate spacecraft and ensure safe landings on Mars [1]. Typically, for robotic Mars surface missions, the spacecraft enters the atmosphere traveling at ∼5.5 km/s and must be slowed down to less than ∼1 m/s at the surface [2,3]. This is achieved through the entry, descent, and landing (EDL) phase of the mission. Every Martian surface mission to date has used a parachute to decelerate the spacecraft during the descent phase of the mission.

Due to the challenges of predicting and testing supersonic parachute performance, previous NASA missions have included large parachute design margins [4,5]. The recent Mars 2020 mission relied on full-scale flight experiments performed during the Advanced Supersonic Parachute Inflation Research Experiments (ASPIRE) to qualify the parachute design [4,6]. The ASPIRE program consisted of a series of high-altitude Earth tests that used a sounding rocket to test parachutes at supersonic Mars-relevant conditions, and three ASPIRE tests were completed (SR01, SR02, and SR03). In addition to qualifying the design for the Mars 2020 parachute, these tests have also provided a large body of reconstructed flight-test data that can help researchers understand the complex dynamics associated with supersonic parachute inflations (e.g., [6,7]). While progress has been made in fluid–structure interaction (FSI) modeling for supersonic parachute inflations [8–12], further model development, validation, and sensitivity efforts are needed before computational tools can be confidently used in the design process of future space missions.

In this work, we focus on modeling the permeability of the broadcloth material used in the Mars 2020 supersonic DGB parachute construction under flight-relevant conditions. Parachute broadcloth material, the primary material used to construct a parachute canopy, is a thin, woven, permeable textile. Experimental permeability measurements for broadcloth are typically made under ambient conditions with the material in a (near) zero stress state, as described in [13–15]. Due to the lack of test data under the expected low-density CO_2 flight conditions on Mars, these experimental data are typically extrapolated to high-altitude Mars conditions [14]. Recent experimental efforts have provided detailed surface characterization measurements for parachute materials, enabling the digital reconstruction of "real" parachute materials [16,17]. These detailed reconstructions are used in the computations of this work, negating

Presented as Paper 2024-4224 at the AIAA Aviation 2024 Forum, Las Vegas, NV, July 29–August 2, 2024; received 21 February 2025; accepted for publication 26 June 2025; published online 31 July 2025.

*Ph.D. Student, Department of Mechanical Engineering, Gateway North Building, Room 017.
†Assistant Professor, Department of Mechanical Engineering, Edwin A. Stevens Hall 323, 1 Castle Point Terrace; jrabinov@stevens.edu. Associate Fellow AIAA (Corresponding Author).
‡Ph.D. Student, Department of Mechanical and Aerospace Engineering.
§Assistant Professor, Department of Mechanical and Aerospace Engineering.
¶Ph.D. Candidate, Aerospace Engineering, 104 S Wright Street.
**Ph.D. Student, Aerospace Engineering, 104 S Wright Street.
††Assistant Professor, Aerospace Engineering, 104 S Wright Street. Senior Member AIAA.
‡‡Ph.D. Candidate, Department of Aeronautics and Astronautics, Durand Building, Room 226.
§§Department of Aeronautics and Astronautics, Durand Building, Room 214.
¶¶Vivian Church Hoff Professor of Aircraft Structures, Department of Aeronautics and Astronautics, Department of Mechanical Engineering, and Institute for Computational and Mathematical Engineering, Durand Building, Room 257. Fellow AIAA.
***Systems Engineer, Jet Propulsion Laboratory, 313H, 4800 Oak Grove Drive.
†††Mechanical Engineer, 352L, 4800 Oak Grove Drive.

the need for simplified or approximate geometries. Simulation results using detailed surface reconstructions can be directly compared to results from simplified geometries and reduced-order permeability models.

The rest of the paper is organized as follows: First, a background and review of the current state-of-the-art for modeling permeability within the scope of supersonic parachutes is discussed in Sec. II. Next, the experimental setup to characterize the fabric and 3D surface reconstruction is discussed in Sec. III. In Sec. IV, the computational tools and methods used to perform the numerical simulations are shown, followed by the results and discussions from those simulations in Sec. V, and conclusions are provided in Sec. VI.

II. Background and Motivation

Textile permeability in the incompressible regime has long been studied due to its significant effects on the aerodynamic behavior of parachutes [18]. However, permeability in a low-density regime, relevant to Mars parachutes, has received considerably less attention in the literature. At low pressure conditions, the mean free path can be of the same order as the characteristic pore size of the broadcloth textile, such that the non-continuum flow effect becomes important in the momentum transport through the porous textile. Currently, textile permeability is typically measured following ASTM D-737 under ambient conditions with no appreciable strain applied to the material. During testing, the average velocity through the material is measured for different differential pressures applied across a test sample (e.g., [13,14]). For Mars parachutes, these Earth-ambient permeability results are then extrapolated to Mars-relevant conditions [14] for use in system-level aerodynamic descent models or FSI simulations. Only recently has detailed surface reconstruction of these materials been successfully completed using X-ray imaging [16], and these reconstructed images provide resolution of the small-scale structure of the broadcloth material (see Fig. 1). Incorporating these small-scale structures into a system-level parachute model is computationally intractable due to the large disparity in length scales between the broadcloth fibers and a full-size parachute (~70–150 μm and ~15 m, respectively). In this work, we use the term "pore" to refer to the visible space in the weave of a material between the tows in Fig. 1.

Previous works have investigated the permeability of materials in compressible/high-Mach number conditions (though thin materials are typically not the topic of study), and only a few studies have incorporated permeability models into parachute FSI simulations. Modifications to Darcy's law are presented in [19], and compressible variations of Darcy's law are investigated in the context of compressible fluid in granular explosives or fluid-injection scenarios in [20,21]. In [22], a homogenized model for multiperforated liners in combustion chamber flow is presented.

Previous full-scale supersonic parachute FSI works have incorporated different computationally tractable homogenized approaches [23–26] for material permeability. In [24], the permeability of a porous surface is incorporated into an immersed boundary method for compressible viscous flow. Source terms are utilized on the surface of a porous boundary, which are based on the Forchheimer equation. In [26], the permeable surface has been modeled with a Darcy–Forchheimer jump condition at the interface. In their method, the solution from the fluid domain is passed to a structural mesh element, and based on the thickness of the permeable surface, a pair element is found on the other side of the surface that aligns with this structural mesh element, and state information is exchanged between the two. Herein, we focus on the reduced-order model previously proposed in [23], where a homogenized permeability model was developed based on an assumption of simplified material pore geometries and a thin surface. This model separated convective and viscous fluxes at the surface and, to calculate viscous effects, assumed that within each pore, a fully developed velocity profile existed (with a no-slip boundary condition). These simplifying assumptions enabled an analytical derivation of viscous source terms that could be added to the Navier–Stokes equation at the interface between the fluid and a thin permeable surface. A convex sum of a fluid–fluid and a fluid–surface convective flux based on the pore sizes in the material was also used for modifying the convective fluxes at the fluid–structure interface. Considering a numerical aerial void fraction of the material, α, the convective flux through the porous wall was modified in [23] to be the weighted average of fluid–fluid and fluid–structure flux as

$$\boldsymbol{F}^{\text{ave}} = \alpha \boldsymbol{F}^{\text{Fluid-Fluid}} + (1-\alpha)\boldsymbol{F}^{\text{Fluid-Structure}} \tag{1}$$

Here, $\boldsymbol{F}^{\text{ave}}$ is the numerical inviscid flux function, and α is the numerical void fraction of the fabric. Some additional investigation of this permeability model was performed in [27]. An update to this model where α is non-constant and determined as a function of the strain state of the material is described in [12], and supersonic parachute FSI inflation simulations are shown to have good agreement with ASPIRE flight data. This simplified permeability model requires several inputs that are specific to a given material, including material thickness, an aerial void fraction value (to be discussed in more detail in later sections), and a pore geometry.

The microscale flow through the parachute material shares geometric and length scale similarities with previous microchannel investigations. In [28], a comparison between applying no-slip and slip boundary conditions in a long microchannel with a constant square cross-sectional area predicted a higher mass flow rate and lower shear force compared to when a slip velocity boundary condition was used. When flow through microchannels with a constriction was investigated, it was found that a non-constant cross-sectional area of the channel resulted in a change in mass flow rate and also pressure loss, compared to a channel with a

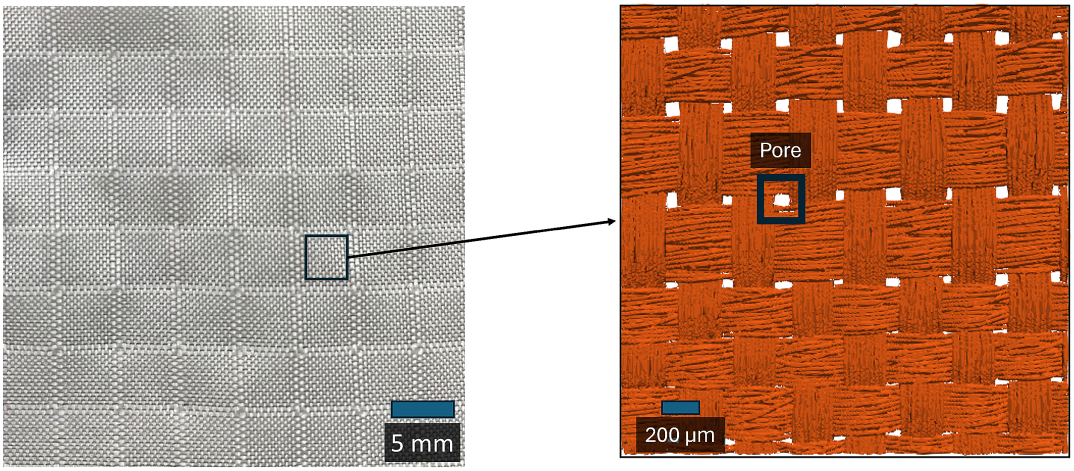

Fig. 1 Image of HFL-G-60315 with ripstop "macro-cells" visible (left) and the detailed reconstruction of the fabric showing small-scale features and an example "pore" (right).

constant cross-sectional area [29]. Their results showed that flow separation occurs in the transition section, but this does not change the pressure distribution. Multiple attempts have been made to find an analytical solution inside a microchannel when the effects of rarefaction and compressibility are significant. A two-dimensional flow analysis with a first-order slip velocity showed that both rarefaction and compressibility effects are important in long microchannels [30]. A second-order slip wall boundary condition was proposed and shown to be more accurate in the higher range of slip regimes and when rarefaction effects are higher [31]. It is important to note that most of the work in this field has been on long planar microchannels and channels with higher aspect ratios (the ratio of the width of the channel to the height of the channel), whereas parachute materials are thin. In [32], airflow through a rectangular cross-section microchannel was investigated in experiments. The numerical simulation for a three-dimensional and two-dimensional channel and comparison to an analytical solution showed a significant change by adding the three-dimensional effects. It was also shown that in a finite-length microchannel, the inlet and outlet reservoirs must be included in computations. The insights gained from these previous works can help guide our studies when rarefied cases are considered. While the parachute material under investigation in this work is much thinner than the typical length of a microchannel considered, some overlapping physical phenomena are still observed between the two geometries.

In this work, we report results from detailed simulations through the microstructure of the Mars 2020 parachute broadcloth material. Results from these small-scale simulations are used to evaluate and compare homogenized permeability models, which are needed for full-scale parachute simulations. To validate the choice of material-specific parameters used in the simplified permeability model in Sec. V.A, Earth ambient CFD results using simplified pore geometries will be compared to experimental data (as was performed in [23]). The velocity profiles inside the pore are compared to an analytical pipe flow solution to see if the assumption of having a fully developed flow is valid. Based on preliminary results shown in [27], there is the potential for rarefied effects when considering Mars atmospheric low-density conditions and length scales comparable to material fibers and pores. Low-Re Low-Density CFD results for simplified pore geometries will be compared to Direct Simulation Monte Carlo (DSMC) simulations [33] results relevant to ASPIRE SR03 flight conditions (Sec. V.B). A CFD (with a no-slip boundary condition, as originally assumed in [23]) to DSMC comparison allows us to investigate whether or not rarefied flow effects, such as an expected non-zero wall slip velocity through the pore, have a significant effect on the overall permeability of the material. DSMC simulations will also be used to compare permeability results using the simplified pore geometries originally proposed in [23] to DSMC results using the detailed reconstructed geometries (Sec. V.C). Finally, counterpart CFD simulations using the homogenized model proposed in [23] are performed to compare to the CFD simplified pore geometry simulations (Sec. V.D).

III. Experimental Setup

A. Material Characteristics

In the present study, we focus on a specific parachute material: HFL-G-60315. It is a modified version of the PIA-C-7020D Type I textile and is the primary material used in the construction of the Mars 2020 parachute canopy and the canopies used in the ASPIRE SR02 and SR03 flight tests [15]. It has a plain woven double-ripstop architecture consisting of equally constructed warp and weft tows of 70 Denier (D) sizing and 20 fibers per tow. Each ripstop tow consists of double the number of fibers and is arranged in pairs. Between each pair of ripstop tows are 14 regular tows. This construction divides the textile into "macro-cells" visible to the naked eye in Fig. 1. The ASTM D-737 standard rated permeability of the textile is 71 $\mathrm{ft}^3/\mathrm{ft}^2/\mathrm{min}$ (CFM) or 36 $\mathrm{cm}^3/\mathrm{cm}^2/\mathrm{s}$.

The permeability of the HFL-G-60315 fabric with plain weave ripstop was measured in a previous study [14]. Testing was conducted using a Textest Instruments FX 3300 Labotester III air permeability tester according to ASTM D-737. Each test utilized quiescent air, with a vacuum pump maintaining a consistent pressure difference across the fabric under examination. The average fluid velocity through the fabric was measured to determine its permeability. Multiple experiments were conducted at various pressure differentials to assess how the averaged velocity changed with pressure drop [13,14]. Experimental permeability data for other parachute materials can be found in [13–15].

B. Three-Dimensional Surface Reconstruction

Using X-ray micro-computed tomography (μCT), images of the parachute fabric under various loads were captured utilizing a 2D tensile tester described in [16]. The apparatus is composed of a nylon clamp and plunger, designed to minimize X-ray absorption. Samples were clamped in contact with the plunger and run through a stepwise load-to-failure scheme. The static load was recorded, and a full tomographic scan was acquired with a pixel size of 1.9 μm/pixel and a field of view (FOV) of ~3.7 mm in both height and diameter. After a scan was completed, the set of images was reconstructed into a tiff stack of slices representing the 3D volume of the scanned region. Semantic image segmentation was applied to separate the warp and weft of the fabric from each other and the background, resulting in a clean reconstruction of the material. Figure 2 shows the reconstructed material used in this study. The data used to perform the 3D reconstruction was obtained by holding the broadcloth material sample in place with a minimal clamping load to replicate standard ASTM D-737 testing conditions.

Figure 2 also shows both the detailed reconstructed geometry (left) and possible simplified pore geometries proposed in [23]. The detailed reconstructed geometry of this fabric showed a repeating pattern of pores inside the fabric. Although different pores with different shapes and sizes are observed in the material, the methodology described in [23] starts by assuming an average unit cell geometry with a simplified shape and void fraction (α) that is related to the average areal porosity of the fabric. In the real parachute material, we expect that the spacing between individual fibers will also contribute to material permeability (in addition to the regularly spaced pores observed between the fiber tows). For the simplified pore geometry considered, the weave patterns are reduced to a single channel at the center of this unit cell (Fig. 2). With this assumption, it is expected that the value of α needed in the simplified numerical model to match the permeability of the physical material will be slightly higher than the observed areal permeability since any fiber-fiber spacing in the real material is consolidated into the channel cross-sectional area. The average thickness of this material is estimated to be ~100 μm based on the reconstructed geometry. The spatial periodicity of the weave pattern of the fabric is, on average, ~400 μm in both directions in-plane. The void fraction based on the areal projection of the fabric is estimated to be ~3%, which is smaller than the numerical α value proposed in Sec. V.

IV. Computational Modeling

Experimental permeability tests are performed under ambient lab conditions where average velocity through the material is measured as a function of applied differential pressure across the material [14]. Based on the gas properties of the air at the time of the experiment, the Reynolds number Re is calculated as

$$Re = \frac{\dot{m} D_h}{A\mu} \tag{2}$$

where A is the cross-sectional area, D_h is the associated hydraulic diameter, and $\dot{m}$ is the mass flow rate, defined as $\dot{m} = \int_A \rho u \, \mathrm{d}A$. For the majority of this work, a Reynolds number based on the unit cell dimensions is used with $D_h = 400$ μm and $A = 0.16$ mm^2. If a Reynolds number based on the pore size is needed, we use the notation Re_p, and this value is calculated with $D_h = 90$ μm and $A = 0.0081$ mm^2. The Knudsen number Kn for each flow

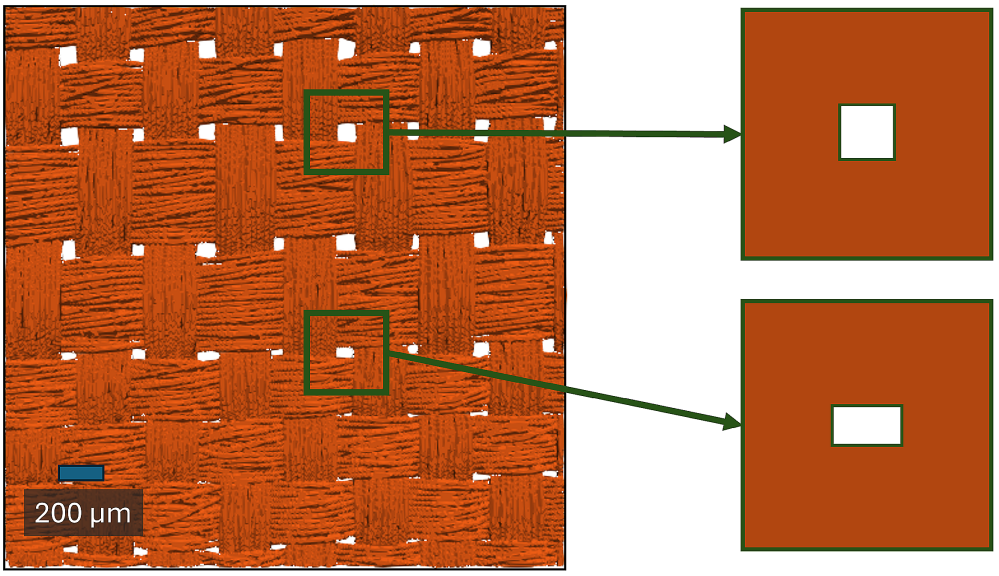

Fig. 2 Detailed reconstruction of parachute material (left) and simplified pore geometries proposed in [23] (right).

condition can aid in estimating the significance of rarefied effects and whether or not a continuum assumption is valid and is defined as

$$Kn = \frac{\lambda}{L} \tag{3}$$

where λ is the mean free path defined in Eq. (4), and L is the characteristic length scale, chosen to be the hydraulic diameter of the pore. Combining the mean free path

$$\lambda = \frac{1}{\sqrt{2}\pi d^2 n} \tag{4}$$

with the number density n,

$$n = \frac{p}{k_B T} \tag{5}$$

yields

$$Kn = \frac{k_B T}{\sqrt{2}\pi d^2 pL} \tag{6}$$

where k_B is the Boltzmann constant, and d is the particle hard-shell diameter, and its value for air is taken from [33] as $d = 4.19 \times 10^{-10}$ m. The typical Prandtl number (the ratio of momentum to thermal diffusivity) is used with $Pr = (c_p \mu/\kappa)$, where c_p is the specific heat at constant pressure and κ is thermal conductivity.

During experimental permeability testing at ambient conditions, the velocities through the material are quite low, and an incompressible flow assumption is expected to be valid. However, in flight-relevant scenarios, due to the lower densities and higher pressure ratios across the parachute surface, supersonic flow is observed. It should be noted that, for the AERO-F simulations, even though they are performed under ASPIRE SR03 relevant conditions, the homogenized model inherently averages all flow quantities, and the mesh resolution is intentionally chosen to be much larger than the pore length scale. Therefore, the local jet structure observed in the pore-resolved simulations is intentionally not captured in the AERO-F simulations. This yields a relatively low magnitude of velocity, consistent with the average velocity of flow through the broadcloth material in the AERO-F simulations.

To perform the CFD simulations, we use the open-source, high-performance computing research library NGA2 [34]. Within NGA2, we use both the incompressible solver [35] for modeling the Earth ambient ASTM D-737 test conditions, as well as the MAST compressible solver [36] for low-density simulations, where compressibility effects are expected to be relevant. The open-source vertex-based finite volume flow solver AERO-F [37–39] is used for the homogenized model simulations. AERO-F is developed and maintained by the Farhat Research Group (FRG) at Stanford University [40] and is used for full-scale supersonic parachute inflation simulations [12]. To perform DSMC simulations, we use the open-source code Stochastic Parallel Rarefied-Gas Time-Accurate Analyzer (SPARTA), primarily developed at Sandia National Laboratories [41,42]. Simulations in this work are performed using NSF ACCESS resources [43] on the Anvil cluster at Purdue University along with computational resources provided by the NASA High-End Computing (HEC) Program through the NASA Advanced Supercomputing (NAS) Division at Ames Research Center. Table 1 provides a summary of the different solvers and flow conditions used and investigated in this work.

A. Low-*Re* High-Density Simulations

Incompressible simulations are performed and compared with experimental data for HFL-G-60315 [14]. In all tests, the upstream flow pressure is set to 94,625 Pa to match the experimental conditions. The laboratory temperature during the experiment was measured at 296.5 K, and the air properties used in the simulations are listed in Table 2. Eight CFD-Incomp simulations are performed using the simplified pore geometry and the NGA2-Incompressible solver to determine if the average velocity from the CFD-Incomp

Table 1 Summary of different sets of simulations performed in the paper

Simulation	Solver	Surface boundary condition	*Re*	*Kn*	*Ma*
Low-*Re* high-density	CFD (NGA2-Incompressible)	Adiabatic, no-slip	1–35	$\ll 1$	$\ll 1$
Low-*Re* low-density	CFD (NGA2-MAST)	Adiabatic, no-slip	1–20	0.03–0.5	0.2–1.8
Low-*Re* low-density	DSMC (SPARTA)	Adiabatic, diffuse	1–35	0.03–0.5	0.2–1.8
Low-*Re* low-density	CFD homogenized (AERO-F)	Adiabatic, no-slip	1–20	$\ll 1$	$\ll 1$

Table 2 Air properties used in the Low-*Re* High-Density simulations

Parameter	Description	Value
R	Gas constant	$287.2\ \mathrm{J \cdot kg^{-1} \cdot K^{-1}}$
μ	Dynamic viscosity	$1.846 \times 10^{-5}\ \mathrm{kg \cdot m^{-1} \cdot s^{-1}}$
ρ	Gas density	$1.111\ \mathrm{kg \cdot m^{-3}}$
T	Temperature	296.5 K
Pr	Prandtl number	0.72

simulations matches the experimental data over a large range of pressure differentials when an appropriate α value is chosen. This is similar to the analysis performed in [23], though a different parachute material is investigated and a different CFD solver is used in this work.

A schematic of the computational domain is shown in Fig. 3. The dimensions of the domain are $2000 \times 400 \times 400$ μm (in the x, y, and z directions, respectively). The y and z dimensions of 400 μm correspond to the approximate unit cell dimensions of the periodic pores observed in the material. A square pore based on the proposed geometries in Fig. 2 is chosen for the simplified geometry. The void fraction is chosen to be 5% (after iteration), which, based on the unit cell size, yields a 90×90 μm square pore (dimensions in the y and z directions, respectively) at the center of the unit cell. The average thickness of the fabric is 100 μm, which is used as the length L of the unit cell. Figure 4 shows a schematic of the pore with dimensions labeled as a and b. The aspect ratio of the pore can be defined as the ratio between a and b, and in this case, $a = b$, as the aspect ratio is 1.

In these CFD-Incomp simulations, a uniform velocity inlet boundary condition is prescribed at the inlet (the upstream side of the fabric), and an outlet condition is specified on the downstream wall.

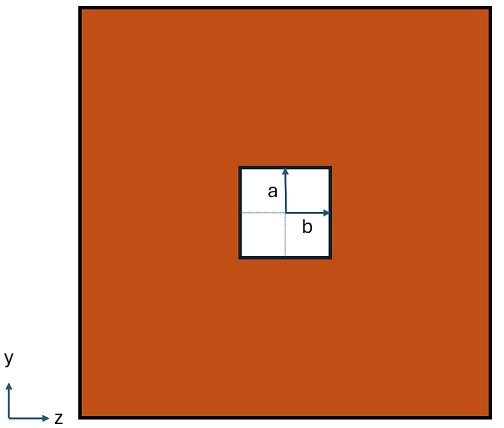

Fig. 4 Simplified square pore geometry.

A symmetry boundary condition is applied in the transverse directions. On the pore surface, a no-slip velocity condition is applied, along with an adiabatic boundary condition. The resulting pressure drop based on the specified inlet velocity is calculated based on the simulation results (it is not specified *a priori*). A list of all the inlet conditions is shown in Table 3. A mesh convergence study is performed to ensure a well-resolved mesh inside the boundary layer at the pore walls. Based on the results of this convergence study (see Appendix A), a grid size of 2.5 μm is chosen for these CFD-Incomp simulations.

B. Low-*Re* Low-Density Simulations

To investigate permeability under Mars-relevant conditions, additional CFD-Comp and DSMC simulations using the same unit cell and simplified pore geometry as before, the reconstructed geometry,

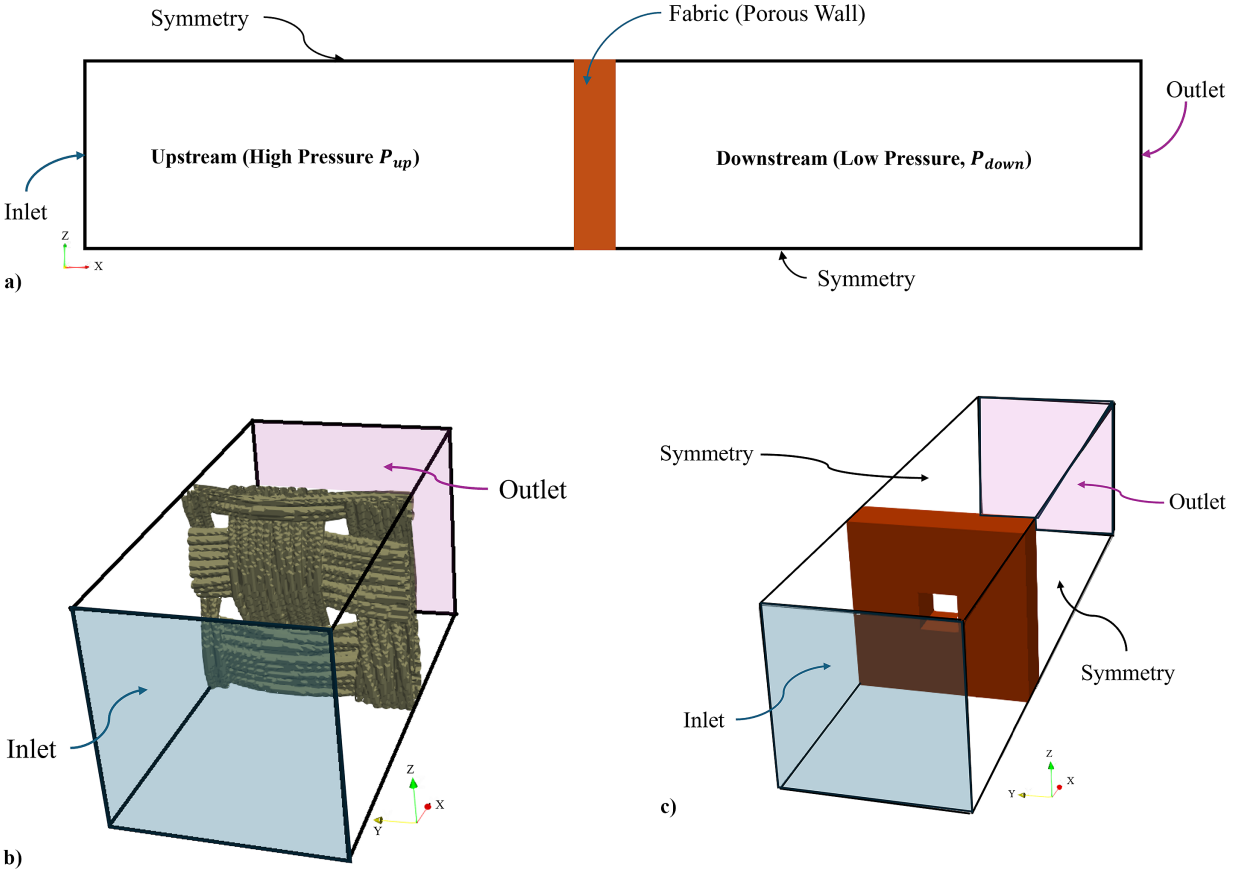

Fig. 3 Computational domains: a) general schematic, b) DSMC reconstructed geometry, and c) simplified geometry used in both CFD-Comp and DSMC simulations (not to scale).

Table 3 Summary of conditions for the Low-*Re* High-Density, CFD-Incomp simulations

Case	Inlet velocity	Pressure difference
A	$u = 0.04\ \text{m} \cdot \text{s}^{-1}$	$\Delta p = 7.9$ Pa
B	$u = 0.06\ \text{m} \cdot \text{s}^{-1}$	$\Delta p = 12.1$ Pa
C	$u = 0.1\ \text{m} \cdot \text{s}^{-1}$	$\Delta p = 20.8$ Pa
D	$u = 0.15\ \text{m} \cdot \text{s}^{-1}$	$\Delta p = 34.1$ Pa
E	$u = 0.2\ \text{m} \cdot \text{s}^{-1}$	$\Delta p = 49.3$ Pa
F	$u = 0.5\ \text{m} \cdot \text{s}^{-1}$	$\Delta p = 191.2$ Pa
G	$u = 1.0\ \text{m} \cdot \text{s}^{-1}$	$\Delta p = 575.7$ Pa
H	$u = 1.5\ \text{m} \cdot \text{s}^{-1}$	$\Delta p = 1131.7$ Pa

Table 4 Air properties used in the Low-*Re* Low-Density simulations

Parameter	Description	Value
R	Gas constant	$287.2\ \text{J} \cdot \text{kg}^{-1} \cdot \text{K}^{-1}$
μ	Dynamic viscosity	$2.33 \times 10^{-5}\ \text{kg} \cdot \text{m}^{-1} \cdot \text{s}^{-1}$
γ	Heat capacity ratio	1.4
c_p	Specific heat at constant pressure	$1018.1\ \text{J} \cdot \text{kg}^{-1} \cdot \text{K}^{-1}$
κ	Thermal conductivity	$0.0333\ \text{J} \cdot \text{s}^{-1} \cdot \text{m}^{-1} \cdot \text{K}^{-1}$
Pr	Prandtl number	0.72

and the homogenized reduced-order model approach are performed in a low-density regime. An ideal and calorically perfect gas is assumed, and Table 4 lists the air properties in the simulations. A constant viscosity is assumed in the CFD-Comp simulations, and the value used is calculated based on Sutherland's law and the specified upstream temperature. The flow conditions are chosen based on expected conditions inside the fully inflated canopy of the DGB parachute during the SR03 test and are approximated based on computational results in [12]. Three values for the estimated pressure ratio (Π), defined to be the ratio of the upstream to downstream pressure across the parachute canopy, are chosen for this work. Under SR03 conditions at peak load, Π is ~15. For an isentropic compressible inviscid air flow, the critical Π that generates a choked flow is ~1.9. The high Π values for flight-relevant conditions significantly change the expected flow regime, as compressible underexpanded jets are expected through each pore. However, due to the low Reynolds number of the flow (small length scales of the pore), viscous effects are expected to be significant, and flow features are expected to differ significantly from a canonical high Reynolds number underexpanded jet [44].

For the unsteady NGA2 CFD-Comp simulations, the dimensions of the domain are $4000 \times 400 \times 400$ μm (in the x, y, and z directions, respectively), and the grid size is 5 μm. To initialize the domain, the upstream region of the pore has high pressure, and the downstream region has low pressure. After iterating on the inlet conditions, the upstream conditions listed in Table 5 are achieved, and the resulting pressure ratio based on the pressure drop across the pore is calculated. A fourth-order Runge–Kutta time integration is used with a viscous CFL number of 0.2, which is more limiting than the convective CFL.

To compare the simplified pore geometry simulation results to the homogenized model in [23], a series of steady-state simulations using AERO-F are performed with the same upstream condition as the NGA2 simulations. A schematic of the computational domain and the porous surface inside the domain is shown in Fig. 3a. Subsonic boundary conditions are prescribed at the inlet and the outlet; Mach number and density are specified at the inlet; and only pressure is specified at the outlet. Air properties are consistent with the simplified pore geometry simulations, referenced in Table 4. The square pore is not resolved, and the homogenized permeability model [23] is applied to an infinitely thin embedded surface that acts as the porous wall. The grid size used in these simulations is 5 cm, which is two orders of magnitude larger than the unit cell used in the simplified geometry. This grid size, along with the solver settings (HLLC approximate Riemann solver with linear flux reconstruction), are taken to match typical settings used in full parachute FSI simulations [12]. However, in this work, steady-state simulations are performed, while full parachute simulations are unsteady.

We apply comparable surface boundary conditions for all of the CFD-Comp and DSMC simulations. However, one significant difference between the CFD-Comp and DSMC simulations is that the CFD-Comp simulations use an adiabatic no-slip velocity boundary condition on the pore surface, while the DSMC simulations use an adiabatic diffuse boundary condition, which allows for a non-zero slip velocity to develop. In SPARTA, subsonic inlet and outlet boundary conditions are used to generate a high-pressure region upstream and a low-pressure region downstream of the material. The same boundary and initial conditions are used for SPARTA simulations with the simplified geometry and with the reconstructed geometries (Fig. 3). Pressure and temperature are specified at the inlet, and only pressure is specified at the outlet. The adaptive mesh refinement capability of SPARTA is used to ensure that the local Knudsen number based on the grid size is <1. The time step was chosen as a fraction of the mean collision time and based on the upstream conditions. For cases 1 through 3, the time step sizes are 5.036×10^{-10}, 2.755×10^{-10}, and 2.455×10^{-10} s, respectively. A variable soft sphere (VSS) model is employed, and when analyzing results, quantities of interest such as density, velocity, pressure, and temperature within each cell are sampled and averaged over 100,000 time steps to reduce statistical fluctuations. Verification for the use of SPARTA for these geometries is provided in Appendix B, where SPARTA simulation results for a 2D microchannel flow are compared to analytical solutions.

V. Results and Discussion

This section provides the results and discussion for all simulations. First, the incompressible results that mimic ASTM D-737 testing are discussed, followed by a discussion of the low-density

Table 5 Upstream conditions, resulting pressure drop, and pressure ratio for all of the low-density simulations

Solver	Case	ρ, $\text{kg} \cdot \text{m}^{-3}$	U, $\text{m} \cdot \text{s}^{-1}$	P, Pa	Pressure drop, Pa	Π	Re
NGA2 CFD-Comp	1	0.0141	1.55	1658	471	1.4	3.7
AERO-F	1	0.0141	1.55	1658	301	1.2	3.7
DSMC-Simplified	1	0.0142	1.83	1693	468	1.4	4.9
DSMC-Reconstructed	1	0.0143	3.07	1705	519	1.4	7.8
NGA2 CFD-Comp	2	0.0215	4.75	2556	2032	4.9	17.4
AERO-F	2	0.0215	4.75	2556	1486	2.4	17.4
DSMC-Simplified	2	0.0212	5.03	2542	2038	5.0	19.5
DSMC-Reconstructed	2	0.0216	7.16	2561	2040	4.9	25.9
NGA2 CFD-Comp	3	0.0232	4.95	2703	2435	10.1	19.7
AERO-F	3	0.0232	4.95	2703	1674	2.6	19.7
DSMC-Simplified	3	0.0231	5.81	2738	2538	13.7	23.1
DSMC-Reconstructed	3	0.0231	8.09	2735	2536	13.8	31.3

results relevant to the supersonic parachute inflation scenarios of interest to this work.

A. Low-*Re* High-Density Results and Discussion

The pressure drop across the pore (simplified geometry—square pore) generates a flow from left to right, and the formation of a jet downstream of the pore is observed. Figure 5 illustrates how the velocity inside the pore varies for different simulations (see Table 3 for simulation details) as the pressure difference between the upstream and downstream sides of the pore is increased, ranging from a difference of 7.9 Pa in Fig. 5a to a difference of 1131.7 Pa in Fig. 5d. For cases with lower pressure drops, the jet expands a shorter distance into the downstream region, but as the pressure drop increases, the jet penetrates further downstream. In the cases with higher pressure drops, the flow does not reach a steady state in the entire computational domain. However, in the region of interest, which is inside and slightly upstream and downstream of the pore, it was found that after 30 μs, the flow reaches a steady state, and the mass flow rate inside the pore converges to a constant value. The average velocity through the pore can be determined from the mass flux. As the flow is incompressible, the average velocity across the surface can be directly compared to experimental data.

Simulation results for all cases are compared to permeability data from [14] in Fig. 6. As numerical results show good agreement with the experimental data, this comparison serves to validate the selection of three key parameters for the simplified pore geometry: a) length of the simplified pore (chosen to be 100 μm), b) shape of the simplified pore (square channel), and c) the numerical void fraction, α, of the unit cell, which for $\alpha = 5\%$ gives us the dimension of the pore as $a = 90$ and $b = 90$ μm. This comparison shows that the choice of a single simplified unit cell is valid for a large range of pressure drops.

As previously discussed, the authors in [23] use Hagen–Poiseuille flow theory (assuming a fully developed flow in a duct) for flow through the pores to calculate the viscous contribution to the homogenized permeability model. For a square duct, as shown in Fig. 4, the following velocity profile $U(y, z)$ has been derived [45]:

$$U(y,z) = \frac{16a^2}{\mu\pi^3}\left(-\frac{\mathrm{d}p}{\mathrm{d}x}\right)\sum_{i=1,3,5,\ldots}^{\infty}(-1)^{\frac{(i-1)}{2}}\left[1-\frac{\cosh(i\pi z/2a)}{\cosh(i\pi b/2a)}\right] \times\frac{\cos(i\pi y/2a)}{i^3} \tag{7}$$

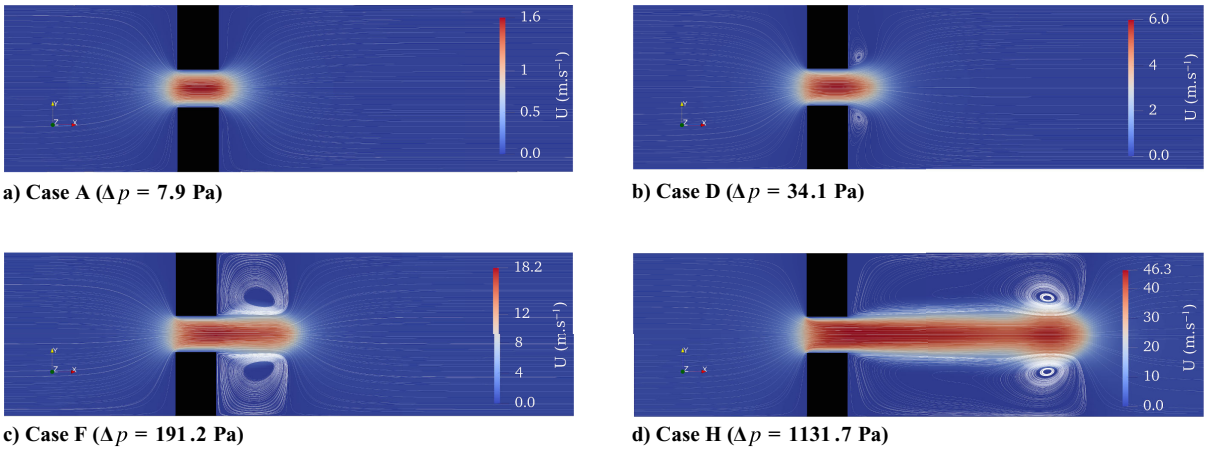

a) Case A (Δp = 7.9 Pa) **b) Case D (Δp = 34.1 Pa)**

c) Case F (Δp = 191.2 Pa) **d) Case H (Δp = 1131.7 Pa)**

Fig. 5 Streamwise velocity in the central *x*–*y* plane (simplified geometry, CFD-Incomp simulations, conditions from Table 3) at $t = 30$ μs. The pressure drop increases from (a) to (d).

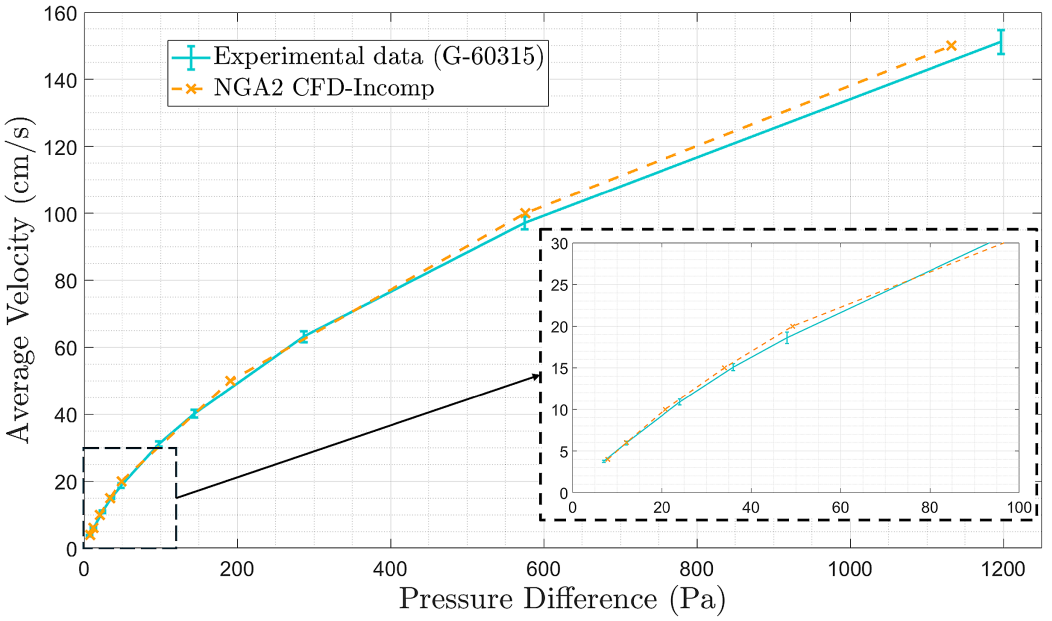

Fig. 6 Permeability results: experimental data [14] and computational results (simplified geometry CFD-Incomp) for $\alpha = 0.05$, square pore, thickness of 100 μm, and a 400 by 400 μm unit cell.

where a is duct half-height and b is duct half-width (Fig. 4). The average pressure at the entrance and exit of the pore is used to find the pressure drop across the pore. Using Eq. (7), the in-plane shear stress on the surface can be evaluated using the off-diagonal components of the shear stress tensor:

$$\tau_{ij} = \mu\left(\frac{\partial u_i}{\partial x_j} + \frac{\partial u_j}{\partial x_i}\right); \quad i \neq j \tag{8}$$

We define $\boldsymbol{f_\tau(n)}$ to be the in-plane force per unit area on a surface with unit vector $\boldsymbol{n}$, and using index notation, this can be expressed as [46]

$$f_{\tau,i} = \tau_{ji} n_j \tag{9}$$

where forces normal to the surface are not included in this expression, to focus on viscous contributions to the drag. The magnitude of force per unit area on the surfaces inside the pore can be found from the vector norm of the components of the force per unit area vector as $\|\boldsymbol{f_\tau(n)}\|$.

Figure 7 shows how the velocity profile evolves in the pore, and a comparison to the analytical solution is also included. If the flow is fully developed, the centerline velocity inside the pore would not change in the streamwise direction. In cases A–E, the centerline velocity inside the pore starts to increase from the entrance of the pore and reaches a fully developed state at approximately $x = 0.75L$. However, as flow reaches the exit and expands downstream, the flow starts to decelerate, and the streamwise velocity at the exit is lower than inside the pore. From cases F–H, the centerline streamwise velocity continues to increase, and the flow never reaches a fully developed state. Due to the relatively large ratio of duct height to the thickness of the broadcloth, the 3D effects near the upstream and downstream sides of the pore also play a significant role. The area changes upstream and downstream of the pore generate flow separation and recirculation bubbles, which can be observed in Fig. 5.

Additional insight can be gained into the validity of the fully developed flow assumption by estimating the entrance length for each set of flow parameters. There are a variety of laminar entrance length correlations available in the literature, and here we report a minimum and maximum range for entrance length from three different models. The correlation proposed in [47] was developed specifically for microchannels, and the correlations from [45,48] were developed for both duct and pipe flows, so the hydraulic diameter of the pore (2a) is used for these two entry length correlations. Table 6 reports the minimum and maximum values from these three correlations for each case investigated. In this table, the dashed line indicates when the estimated entrance length is greater than the pore thickness.

The Reynolds number for the analytical solution, Re_p^{AN}, can be calculated using Eqs. (2) and (7). For determining the expected entrance length based on CFD-Incomp results, Re_p^{CFD} is used, which is calculated based on the mass flux inside the pore from the CFD-Incomp simulations using Eq. (2).

From Table 6 it can be seen that the development length for lower pressure drop values is smaller than the thickness of the broadcloth, consistent with the previously discussed observations of fully developed flow occurring in the pore for some cases. Although the flow inside the pore is significantly different from the steady-state analytical solution (e.g., see the velocity profile shown in Fig. 7 and shear stress in Fig. 8), if a consistent pressure drop is observed across a resolved pore and a surface using the homogenized model, then the predicted drag is expected to be comparable.

A similar entrance and exit effect was observed when examining the shear stress on the surfaces inside the pore. Assuming the analytical solution for a fully developed flow in a duct, the surface shear yields a uniform distribution from the start to the end of the pore. Figure 8 shows the values of $\tau_{\mathrm{diff}} = \tau_{\mathrm{CFD}} - \tau_{\mathrm{AN}}$. The numerical shear stress results indicate that there is an increase in the magnitude of shear stress at the entrance and exit of the pore, while

Table 6 Values of estimated minimum and maximum development length and Re_p for all CFD-Incomp simulations (the pore thickness is 100 μm for all cases)

Case	L_{entrance} (min – max), μm	$L_{\mathrm{entrance}}^{\mathrm{CFD}}$ (min – max), μm	Re_p^{AN}	Re_p^{CFD}
A	57.6–65.4	55.9–63.2	4.7	4.2
B	67.4–76.9	62.9–72.1	7.3	6.2
C	93.5–102.8	81.0–90.8	13.1	10.4
D	130.9–140.6	103.9–113.5	21.6	15.5
E	177.9–192.9	126.8–136.6	31.7	20.7
F	570.3–686.2	275.1–305.6	118.1	51.8
G	1582.8–2000.1	532.8–761.1	345.7	131.1
H	3002.8–3846.8	737.3–903.1	664.8	155.7

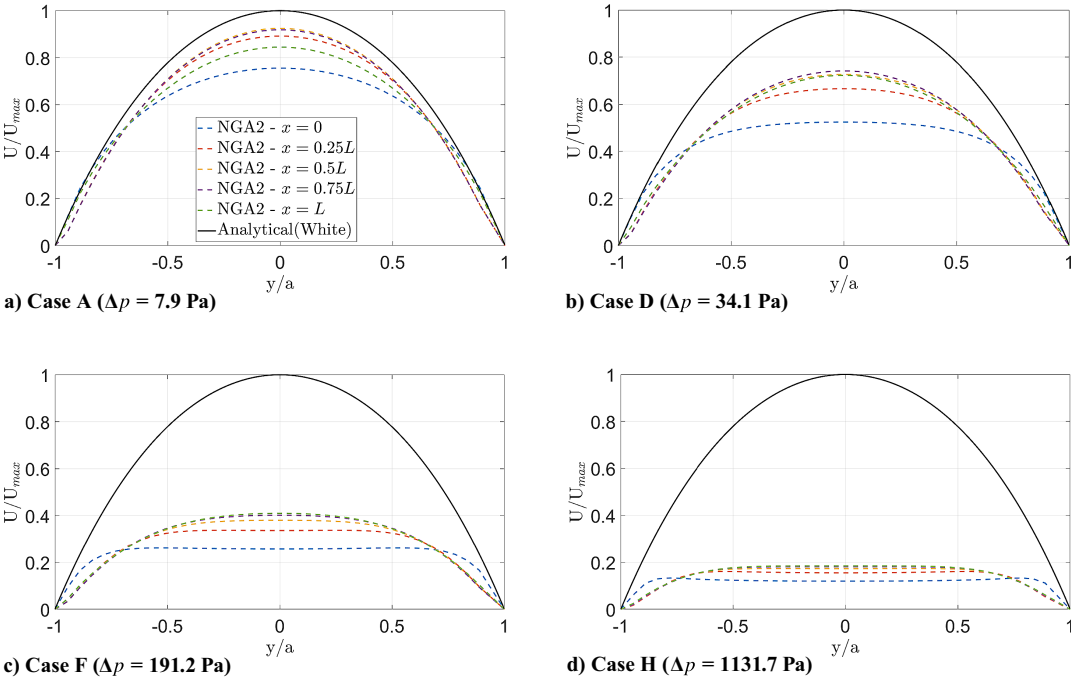

a) Case A (Δp = 7.9 Pa) b) Case D (Δp = 34.1 Pa)

c) Case F (Δp = 191.2 Pa) d) Case H (Δp = 1131.7 Pa)

Fig. 7 Velocity profiles inside the pore computed using simplified geometry numerical simulations.

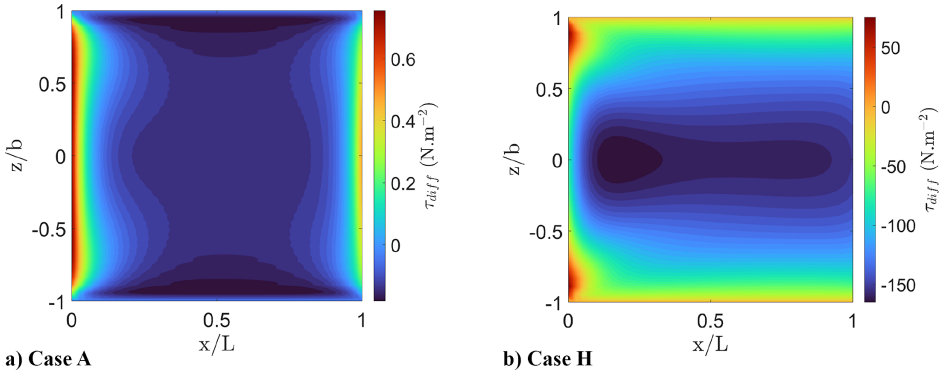

Fig. 8 Difference between shear stress on the pore in the x–z plane computed using the analytical solution [45] and numerical simulations.

Table 7 Values of drag forces for all CFD-Incomp Low-*Re* High-Density cases

Case	F_τ^{CFD}, N	F_τ^{AN}, N	% Diff	$\frac{F_\tau^{\mathrm{CFD}}}{F_P^{\mathrm{CFD}}} \cdot 100\%$	F_D^{CFD}, N	F_D^{AN}, N	% Diff
A	4.12×10^{-8}	4.34×10^{-8}	5.33	5.01	8.64×10^{-7}	8.66×10^{-7}	0.23
B	6.02×10^{-8}	6.71×10^{-8}	11.29	4.74	1.33×10^{-6}	1.34×10^{-6}	0.75
C	1.05×10^{-7}	1.21×10^{-7}	14.28	4.61	2.38×10^{-6}	2.40×10^{-6}	0.84
D	1.61×10^{-7}	1.99×10^{-7}	24.37	4.28	3.94×10^{-6}	3.98×10^{-6}	1.01
E	2.17×10^{-7}	2.92×10^{-7}	34.56	3.91	5.75×10^{-6}	5.83×10^{-6}	1.39
F	5.97×10^{-7}	1.09×10^{-6}	82.57	2.89	2.11×10^{-5}	2.17×10^{-5}	2.84
G	1.29×10^{-6}	3.18×10^{-6}	146.51	2.13	6.16×10^{-5}	6.35×10^{-5}	3.89
H	2.02×10^{-6}	6.11×10^{-6}	202.47	1.74	1.18×10^{-4}	1.23×10^{-4}	4.23

the magnitude of the shear stress at the center of the surface is lower than the analytical solution. The difference becomes more significant as pressure drops increase and the separation and recirculation effects start to play a more significant role.

One of the primary quantities of interest for a parachute is the drag force. The drag force, $F_D = \boldsymbol{F} \cdot \hat{\boldsymbol{e}}_{\boldsymbol{x}}$, is defined as the force on the surfaces of the pore in the streamwise direction. We can find F_i, which is the force on the surfaces from the following:

$$F_i = -\int_A p n_i \, \mathrm{d}A + \int_A \tau_{ji} n_j \, \mathrm{d}A \tag{10}$$

The first term in Eq. (10) is the drag force due to the pressure drop (F_P) across the pore, and the second term is the shear force on the pore surfaces (F_τ). In Table 7, it is shown that F_P is the prominent component of F_D, and shear force is only a few percent of the total drag force. The difference between the analytical solution and the numerical results can be defined as

$$\%\mathrm{Diff} = \frac{|F^{\mathrm{CFD}} - F^{\mathrm{AN}}|}{F^{\mathrm{CFD}}} \times 100 \tag{11}$$

At the lowest pressure drops, the viscous drag calculated from the CFD-Incomp simulation is only ~5% lower than the value predicted from the analytical solution, but at the highest pressure drop, the viscous drag calculated from the CFD-Incomp simulations is lower by ~200%. Even though viscous shear stress differs significantly, it has a minimal effect on the overall drag prediction, as assuming a fully developed flow only changes the F_D values by 0.2–4.2%. Therefore, the fully developed assumption in the reduced-order permeability model in [23] has little effect on the overall drag prediction, presuming that the pressure drop across the material is still captured accurately.

B. Low-*Re* Low-Density Results and Discussion

Similar to the incompressible cases, for the Low-*Re* Low-Density simulations, a jet forms downstream of the pore, though this is now a compressible jet, with some conditions yielding supersonic flow. Figure 9 shows that the Mach number increases as the pressure ratio increases. In Case 1, when the pressure ratio is 1.4, the flow stays subsonic everywhere, while for Cases 2 and 3, when the pressure ratios are 4.9 and 13.7, respectively, the flow becomes supersonic. Both of these pressure ratios are significantly above the isentropic choked flow value of ($\Pi \sim 1.9$) for air. The Knudsen number was calculated to investigate whether rarefied effects are expected to be significant and to investigate whether results from a continuum CFD solver are expected to be valid in this regime. Considering all cases investigated, $0.05 < Kn < 0.7$, so the flow is rarefied and within the slip flow regime or transition regime. In Case 1, Kn remains below 0.1 throughout the entire domain, validating the use of a CFD solver except that slip is still observed on the pore walls. As the pressure ratios increase, the Knudsen number continues to increase, though it remains <0.7, and continuum solutions are expected to be less accurate. Consequently, employing the Navier–Stokes solver to model flow within the pores may introduce errors, especially for cases with higher pressure ratios.

The velocity profiles inside the pore for the CFD-Comp and DSMC simulations are plotted in Fig. 10 for Case 2. In the DSMC simulations, we see a significant slip velocity on the walls. The centerline velocity is also higher for the higher Π cases with a nonzero slip velocity on the walls compared to the CFD-Comp results with a no-slip wall. As will be discussed later in Sec. V.D, because of the slip velocity in the DSMC simulations, the mass flux is higher compared to the CFD-Comp simulations.

Following the same assumption made in [23], analytical shear stresses can be found from Eqs. (7) and (8) numerical results can be extracted from the simulations. The numerical results indicate lower shear stress in DSMC simulations compared to the CFD-Comp simulations. The 3D effect at the leading edge and exit of the pore is shown to change the shear stress distribution, affecting the overall viscous drag force on the pore surfaces in each case. Figure 11 shows the difference between the results from the simulation and from the analytical solution. Total drag forces on the pore are calculated using Eq. (10) and are shown in Table 8. As before, the pressure drag is significantly higher than the viscous drag, with the latter contributing <3% to the total drag force.

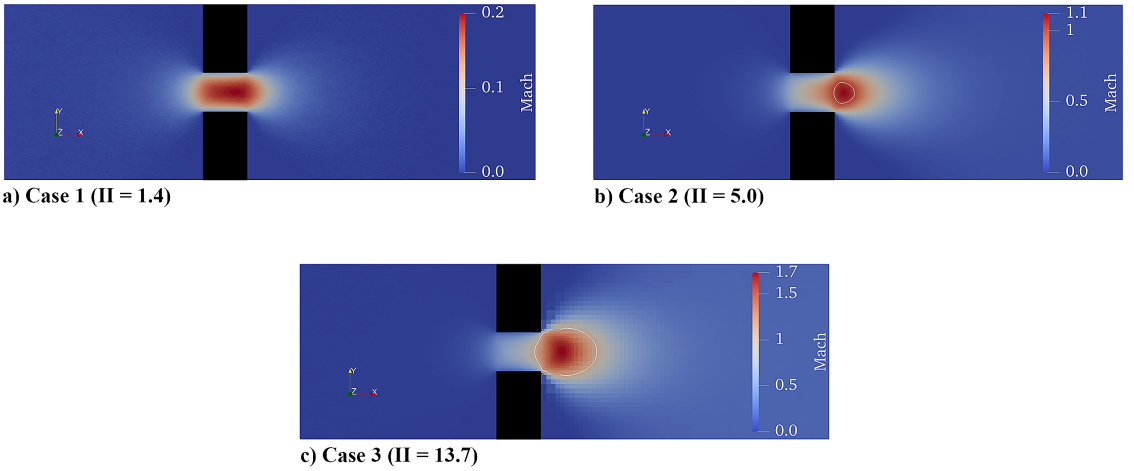

a) Case 1 (II = 1.4)

b) Case 2 (II = 5.0)

c) Case 3 (II = 13.7)

Fig. 9 Mach number from SPARTA DSMC simulations in the x–y plane computed using the simplified geometry. Sonic line ($Ma = 1$) shown with a white contour.

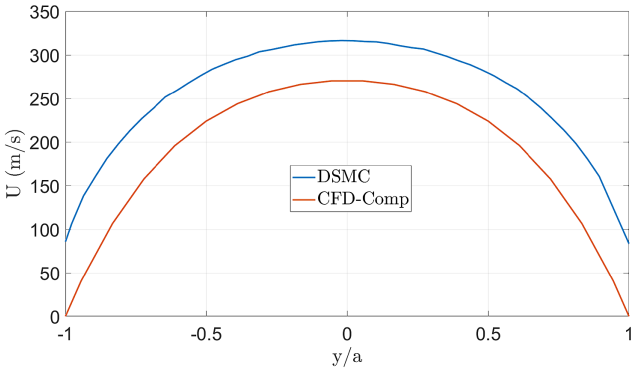

Fig. 10 Slip and no-slip velocity profiles inside the pore at $x = 0.75L$ in the simplified geometry simulation for Case 2.

C. Detailed Reconstructed Geometry

The reconstructed geometry, which gives us a more detailed representation of the fabric, is used for a separate set of DSMC simulations under ASPIRE SR03 relevant conditions. A subsection of the reconstructed geometry is chosen to represent the fabric due to computational cost, and there are four distinct pores in this subsection, which are shown in Fig. 12. As each pore is geometrically different, we see different velocity profiles downstream of each pore, and the extent to which the jet expands downstream increases with the size of the pore, as shown in Fig. 13. Figure 14 shows that the maximum centerline velocity inside the simplified pore is slightly higher than the smallest pore and slightly lower than the largest pore but generally in good agreement with the average velocity of all the pores. However, a discrepancy in streamwise velocity is seen upstream and downstream of the pores. This discrepancy in velocity is largely due to the three-dimensionality of the flowfield when the reconstructed geometry is used compared to the simplified geometry. Furthermore, in the simplified geometry, the thickness of the pore is chosen to represent the average thickness of the fabric with two tows. In the reconstruction, while the fabric maintains the same average thickness, the local thickness of the fabric through a pore is only the thickness of ~1 tow and is approximately ~50 μm, which is smaller than the average thickness of the material, causing the flow to pass through a narrower pore across the fabric. This is also a likely contributor to the discrepancies observed in the streamwise velocity between the two geometries.

To further study the effects of the pore thickness on the flow through the pore, multiple simulations with a simplified square pore geometry are completed, where thickness is in the range of 50–100 μm, and the results are shown in Appendix C. The results show that the discrepancies in the streamwise velocity profile upstream of the pore are still observed compared to the reconstructed geometry results.

As shown in Table 8, the viscous drag force for the simplified and reconstructed geometry results remains at <5% of the total drag force. Different flow structures are observed for both of these geometries. In the reconstructed geometry, there are some complex small-scale 3D geometrical features due to the woven nature of the material, and this geometrical complexity is not present when a simplified geometry is used. This likely changes the flow features observed downstream of the pore, and a more well-defined recircu-

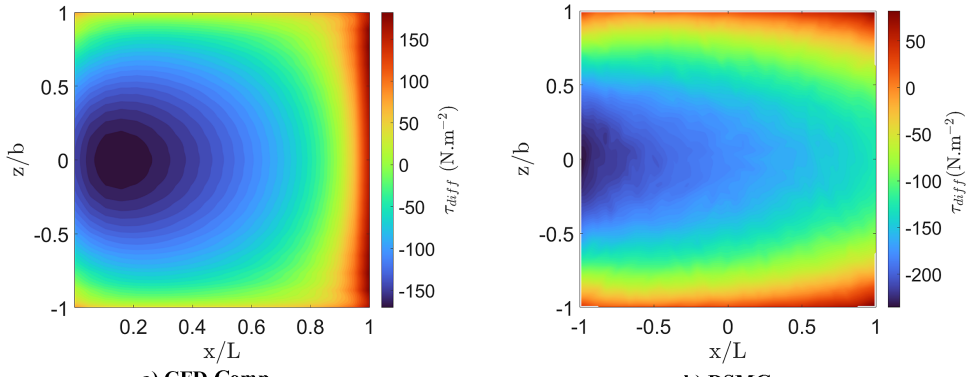

a) CFD-Comp

b) DSMC

Fig. 11 Difference between shear stress on the pore in the x–z plane computed using the analytical solution and numerical simulations for Case 2 with simplified geometry.

Table 8 Values of drag forces for Low-*Re* Low-Density simulations

Solver	Case	F_τ, N	F_τ^{AN}, N	% Diff	$\frac{F_\tau}{F_P} \cdot 100\%$	F_D, N
CFD-Comp	1	2.21×10^{-6}	2.38×10^{-6}	7.7	3.0	7.81×10^{-5}
DSMC-Simplified	1	1.81×10^{-6}	2.24×10^{-6}	23.7	2.4	7.78×10^{-5}
DSMC-Reconstructed	1	1.88×10^{-6}	— —	— —	2.3	8.31×10^{-5}
CFD-Comp	2	8.16×10^{-6}	9.84×10^{-6}	21.7	2.5	3.29×10^{-4}
DSMC-Simplified	2	7.28×10^{-6}	9.86×10^{-6}	35.1	2.2	3.30×10^{-4}
DSMC-Reconstructed	2	6.35×10^{-6}	— —	— —	1.9	3.27×10^{-5}
CFD-Comp	3	9.08×10^{-6}	10.48×10^{-6}	15.5	2.4	3.88×10^{-4}
DSMC-Simplified	3	8.24×10^{-6}	10.52×10^{-6}	27.7	2.1	4.06×10^{-4}
DSMC-Reconstructed	3	7.02×10^{-6}	— —	— —	1.7	4.06×10^{-4}

DSMC-Reconstructed values are normalized by the ratio of the cross-sectional area of the computational domains.

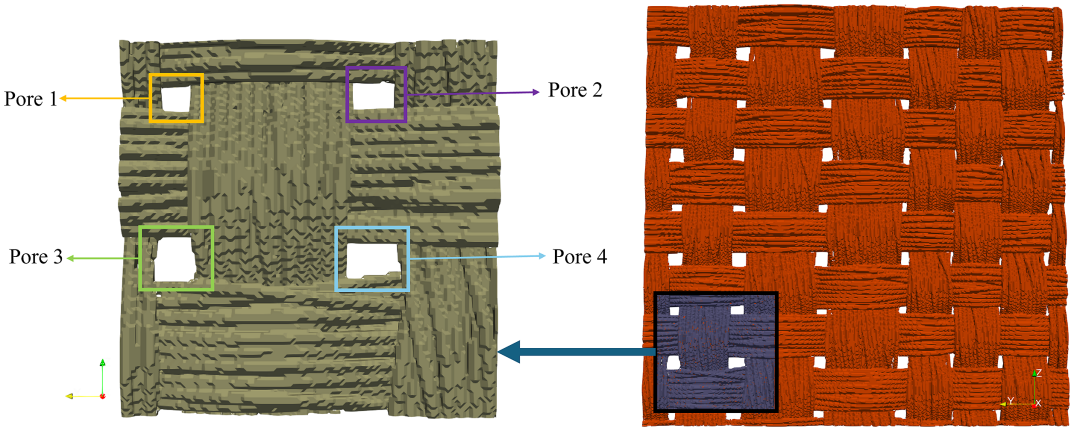

Fig. 12 Left: pore labels for the subsection of the reconstructed geometry used in DSMC simulations. Right: full reconstructed geometry.

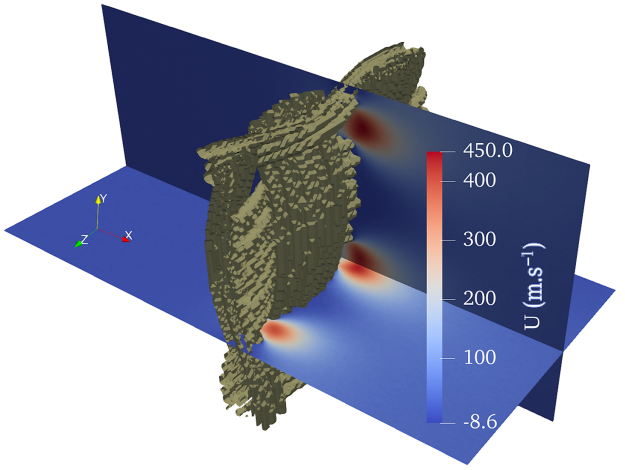

Fig. 13 Velocity profile inside the domain in the reconstructed geometry simulations for Case 2.

lation region is observed in the simplified geometry simulations, as shown in Fig. 15.

As will be discussed in Sec. V.D, the mass flux in the reconstructed geometry is higher than the simplified pore simulations. Multiple factors may contribute to this, such as neglecting the intra-tow porosity that exists in the reconstructed geometry between fibers, as this is not directly modeled in the simplified geometry. In addition, due to computational cost considerations, only a small coupon of the reconstructed fabric was chosen as the surface for the reconstructed geometry simulations. Larger pores are visible in the chosen section of the reconstructed geometry compared to different sections of the entire fabric. Most importantly, the part of the fabric used in the current simulations has a higher areal void fraction, $\alpha = 5\%$, compared to the entire fabric where $\alpha = 3\%$. This highlights the complexity of using the reconstructed geometries where spatial material variations are expected, and future work could investigate how spatially varying permeability may affect simulation results. In the future, the ability to compare low-density simulation results to future experimental data taken under comparable low-density flight-relevant conditions would support beneficial validation efforts.

D. Comparison with Homogenized Model

Steady-state simulations are used in order to compare CFD-Comp and DSMC simulation results in this work, unlike in [23], where an unsteady shock was used. This choice is driven by the challenges associated with modeling unsteady shocks with the DSMC framework [49,50]. The steady-state setup allows the mass flux to be controlled by the chosen simulation parameters, and the pressure drop across the surface is a simulation output. Additional comparisons were performed between NGA2 and AERO-F with an unsteady shock impinging on the permeable surface (similar to the comparison performed in [23]), and the pressure drops across the surface (along with the drag) agree within <5% between the NGA2 CFD-Comp simulation using the simplified geometry and AERO-F using the homogenized permeability model. The discussion below, which focuses on the steady-state results presented in this work, therefore highlights the discrepancies based only on steady-state simulations.

Figure 16 shows mass flux as a function of pressure drop across the permeable surface for all of the low-density simulations. Consistent with [23], a linear relationship between mass flux and pressure drop under these flow conditions is observed. To further assess the influence of the viscous source terms in the AERO-F homogenized simulations, an analytical Euler solution is included

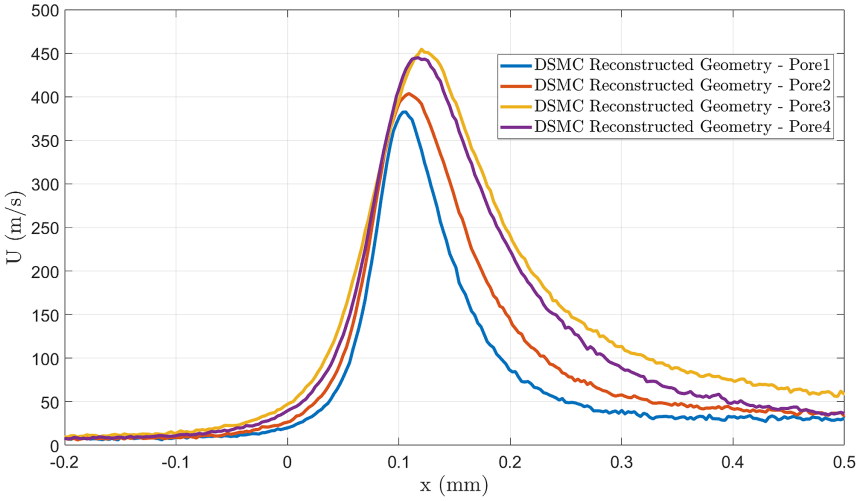

a) Individual pores

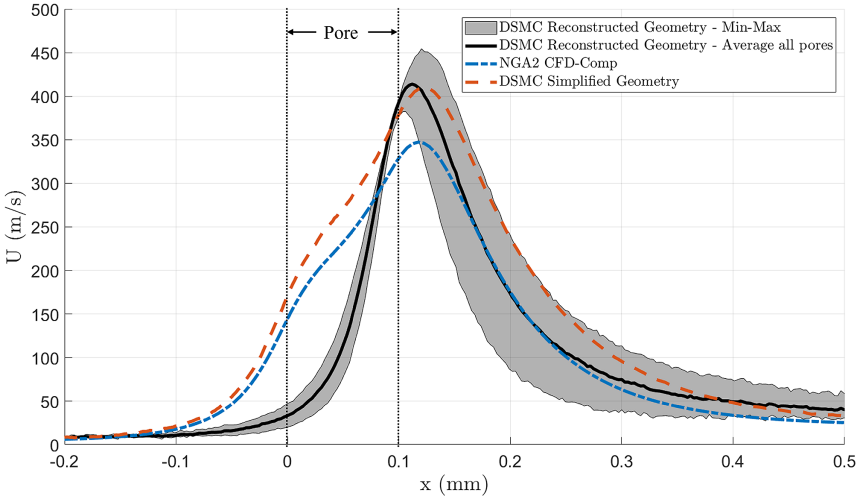

b) Comparison to CFD-Comp and DSMC-Simplified

Fig. 14 Centerline velocity comparison between the simplified and reconstructed geometry simulations for Case 2.

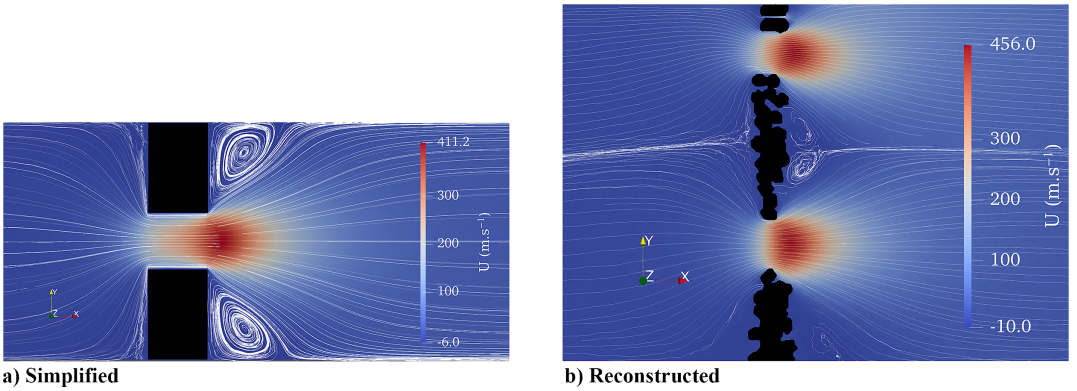

a) Simplified b) Reconstructed

Fig. 15 Velocity profile in the *x*–*y* plane and streamlines for DSMC-Simplified and reconstructed geometries for Case 2.

based on only the convective fluxes from Eq. (1). For the analytical solution, a steady-state solution is found using a standard Godunov method where the fluxes are calculated based on the analytical solution to the local Riemann problem at cell faces [51]. As expected, the viscous source term has a small effect on the overall mass flux, and the analytical solution shows good agreement with the AERO-F viscous homogenized solution. For the homogenized AERO-F results with a steady-state initialization, for the same upstream conditions, there is a lower pressure drop across the surface compared to the simplified pore geometry simulations, though the AERO-F results are bounded between the reconstructed geometry results and the simplified pore geometry results. The mass flux for flow through the simplified geometry is consistently higher for a given pressure drop for the DSMC-Simplified results compared to

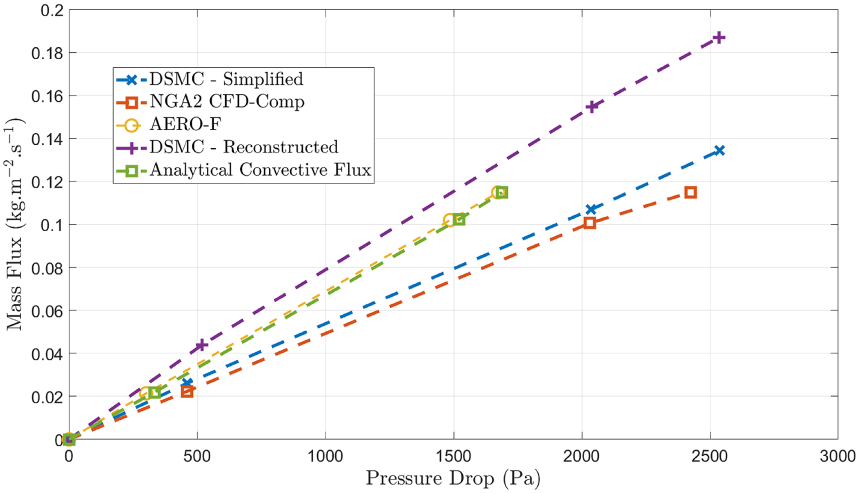

Fig. 16 Comparison of mass flux values as a function of pressure drop for all of the low-density simulations.

the NGA2 Compressible results. While both of these simulations use the same simplified geometry, the non-zero wall slip velocity in the DSMC simulations results in a higher mass flow rate through the pore. Finally, the consistently higher mass flux through the reconstructed geometry compared to all other models is attributed to the locally higher α for the specific area of the reconstructed geometry that was used in these simulations.

The total drag generated by the surface is found from Eq. (10), and results for all the simulations in this study are compared in Fig. 17. The pore-resolved simulations with the simplified geometry (both CFD and DSMC) yield a higher drag force per unit area for a given Reynolds number compared to the homogenized model, which predicts ∼35% lower drag for the same upstream conditions. Using the reported parachute drag and the projected parachute area near peak inflation for the SR02 and SR03 flight tests from [52], an approximate range of drag-to-projected-area values can be calculated. Due to the parachute deployment conditions, this ratio is higher for SR03 compared to SR02 (∼1750 and ∼1400 $\mathrm{N}\cdot\mathrm{m}^{-2}$, respectively). This approximate normalized drag range indicates that the conditions used for the simulations span a representative flight regime for Mars parachutes. However, it is not trivial to extrapolate from the small-scale simulation results presented in this work to the effect that permeability assumptions have on full-scale supersonic FSI parachute inflation simulations. Consistent with [23], it was verified that when an unsteady shock impinges on a permeable surface (generating a reflected shock and a transmitted shock), the pressure drop that is realized across the surface is consistent between the AERO-F homogenized results and the NGA2 CFD-Comp simulations using a simplified square pore. However, for this unsteady configuration, there is a large discrepancy in mass flux between the CFD pore-resolved results and the homogenized simulation results. As the overall drag is dominated by pressure drag, as long as a consistent pressure drop is set up across the fabric, even if the mass flux is different between different solvers/models, the overall drag value is expected to be consistent. Therefore, it is possible that the observed discrepancy in mass flux may not have a large influence on the drag on the surface (or on a full 3D parachute). However, in this work, steady-state flow conditions are investigated, and for a given Reynolds number, it is found that the pressure drop across the surface can vary significantly based on the modeling framework. During parachute inflations, which are transient events (on parachute-scale length scales), it is challenging to determine how significant of an impact the permeability model will have in setting up the pressure drop across the canopy, as this is a complex three-dimensional unsteady flow. While our results do suggest that parachute FSI simulations could be sensitive to the assumed permeability model, detailed sensitivity studies with full FSI simulations will be required to verify this.

Currently, the only experimental permeability data available are gathered from experiments that are performed under Earth ambient conditions with minimal load. Future work that enables permeability measurements to be performed under low-density conditions

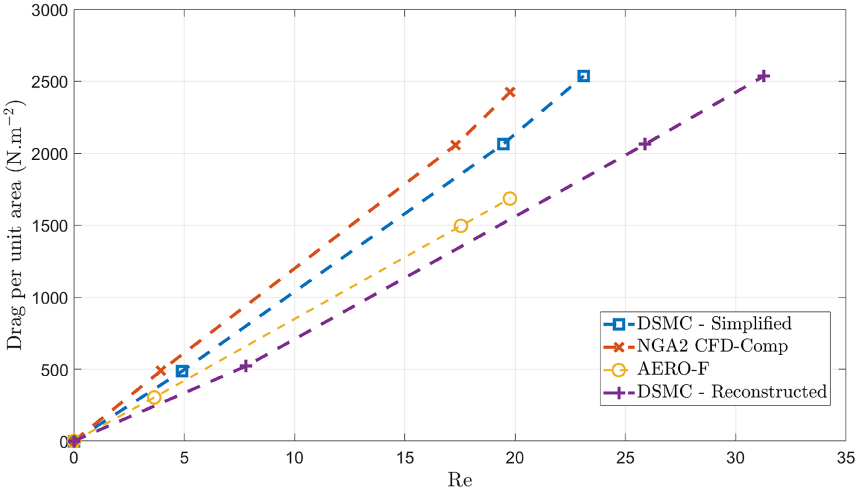

Fig. 17 Comparison of drag per unit area values for *Re* between NGA2 CFD-Comp, DSMC, and homogenized AERO-F results.

and/or under load, conditions relevant to a parachute during inflation, would be extremely valuable for future modeling efforts. Specifically, low-density permeability experiments would enable the validation of the homogenized model under flight-relevant conditions, and experimental permeability data acquired under various loads would enable model validation for the effect of load on permeability (preliminary investigations of this effect have been performed in [12]).

VI. Conclusions

The assumptions outlined in [23] to build a reduced-order model for the permeability of parachute fabric are investigated. The same methodology is used to find an equivalent simplified pore geometry based on incompressible experimental test data for a different parachute material (HFL-G-60315). A comparison between high-density subsonic simulation results and experimental test data shows good agreement and validates the selected pore unit cell size and shape. The velocity profiles and total drag forces indicate a difference between the simulation results and the analytical solution for a fully developed pipe flow. In the simulations, the 3D nature of the flow is observed, and flow separation and recirculation phenomena are present. These effects become more significant as the pressure drop across the pore increases. Despite lower shear forces calculated in the simulations compared to the analytical solution used in the reduced-order model, as the total drag force is predominantly governed by pressure drag, the observed discrepancies in viscous forces only change the total drag force by $\sim$1%.

To investigate permeability under low-density conditions relevant to supersonic parachute inflations at Mars, a series of CFD and DSMC simulations were conducted under ASPIRE SR03 relevant conditions. The flow remains subsonic for the lowest pressure ratio but reaches $\sim Ma = 1.7$ downstream of the pore for the highest pressure difference considered. Evaluation of the Knudsen number reveals that slip is expected at the wall for all cases. There is an observed discrepancy in the mass flow rate between the CFD and DSMC simulations, which could be caused by the assumption of a no-slip wall in the CFD simulations. In all cases, again, pressure drag dominates viscous drag.

By comparing the results from the simplified geometry simulations to reconstructed geometry simulations under low-density conditions, we find some discrepancies in velocity profiles and force predictions. The non-constant pore geometries in the reconstructed surface yield variations in the streamwise velocities through the center of each pore, and more 3D flow features are present compared to the simplified geometry simulations. Consistent with previous works, mass flux varies linearly with pressure drop for all of the low-density scenarios considered in this work.

Overall, the results presented in this work confirm that the assumptions from [23] yield a reduced-order model that is appropriate for capturing broadcloth permeability in a full-scale FSI simulation. The reduced-order model results generally show good agreement with the pore-resolved simulations, with some minor discrepancies observed in predicted drag. To determine whether these discrepancies have a significant effect on modeling supersonic parachute inflations, future sensitivity studies utilizing full-scale parachute FSI simulations are required. While this study focused on the Mars 2020 parachute broadcloth material, the framework presented in this work can be used to determine permeability modeling parameters for other parachute fabrics, once experimental permeability data is available. Future modeling efforts should investigate how spatially varying permeability in the reconstructed geometry affects simulation results; future experimental work that performs permeability measurements under low-density and loading conditions relevant to Mars supersonic parachute inflations would provide valuable data for future model validation efforts.

Appendix A: Mesh Study

A mesh convergence study was conducted for an incompressible NGA2 simulation based on the conditions in Case D from Table 3. Five different mesh sizes (2.5, 5, 9, 11.25, and 15 μm), corresponding to 36, 18, 10, 8, and 6 cells across the pore, respectively, are used. The corresponding axial centerline velocity plots are shown in Fig. A1, and as expected, a second-order convergence is observed (Fig. A2). The error is calculated based on the L_∞ norm as

$$\|U_\infty\| = |U_{\text{finest}} - U_h| \tag{A1}$$

where $U_h = \max(U_h(x, 0, 0))$ is the maximum velocity in the x-direction along the centerline for a given grid spacing h, and U_{finest} corresponds to the results with a mesh spacing of $h = 2.5$ μm. The maximum centerline velocity for each grid size and the calculated error from Eq. (A1) are shown in Table A1.

Appendix B: DSMC Verification

To find the analytical solution for a microchannel in the slip regime, a slip-wall boundary condition can be defined as [53]

$$U\Big|_{\text{wall}} = \frac{2 - \sigma_m}{\sigma_m} \lambda \frac{\partial U}{\partial y}\Big|_{\text{wall}} \tag{B1}$$

where σ_m is the tangential momentum accommodation coefficient, which can vary from zero (specular) to one (full accommodation). Analytical solutions for velocity and mass flow rate in a straight, high-aspect-ratio microchannel for a given pressure ratio have been previously proposed as [29,53]

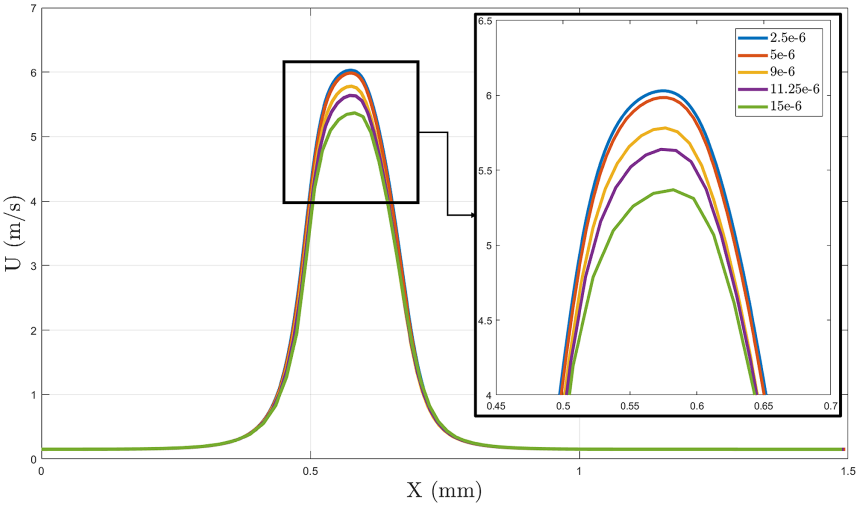

Fig. A1 Comparison of the centerline velocity for different mesh grid sizes for NGA2 CFD-Incomp Case D.

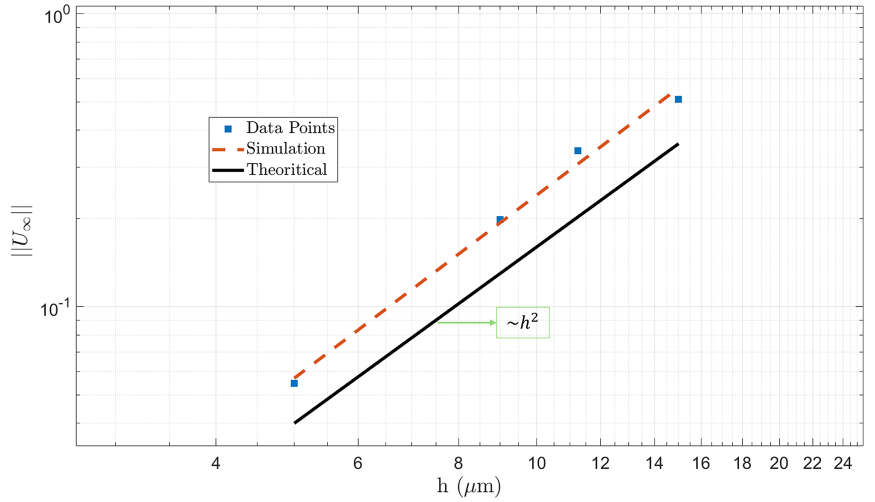

Fig. A2 Centerline velocity convergence for NGA2 CFD-Incomp Case D mesh sensitivity study showing second-order convergence.

Table A1 Low-*Re* High-Density NGA2 CFD-Incomp Case D mesh convergence study results

Grid size, μm	Points across pore	Max centerline velocity, m · s^{-1}	% Difference
2.5	36	6.0303	— —
5	18	5.9754	0.91
9	10	5.8323	3.28
11.25	8	5.6900	5.64
15	6	5.5199	8.46

$$U(x) = \frac{1}{2\mu}\frac{\mathrm{d}p}{\mathrm{d}x}\left(y^2 - \frac{H^2}{4} - H^2 Kn\frac{2-\sigma}{\sigma}\right) \tag{B2}$$

$$\dot{m} = \frac{H^3 w P_o^2}{24\mu L_c RT}\left(\Pi^2 - 1 + 12\frac{2-\sigma}{\sigma}Kn_o(\Pi - 1)\right) \tag{B3}$$

where H is the height, w is the width, and L_c is the length of the channel. These solutions were shown to be valid for a high-aspect-ratio microchannel where the width of the channel is significantly larger than the height of the channel, and the geometry of the channel can be assumed to be 2D [29]. To verify SPARTA results under rarefied microchannel conditions, a 2D channel test with a constant cross-sectional area was performed based on the conditions described in [53]. When the channel walls are prescribed with a full accommodation boundary condition ($\sigma_m = 1$), the velocity profile and the slip velocity on the wall show a good agreement with the analytical solution (Fig. B1). The slip velocity at the wall is significant compared to the maximum velocity at the centerline. In the case with $\sigma_m = 0.85$, as expected, the slip velocity at the wall increases compared to a wall with a full accommodation, and hence the centerline velocity is also higher. The pressure drop across the channel also shows the same non-linear decrease from the inlet to the outlet (Fig. B2) as the analytical solution. Similar small discrepancies between the numerical results and the analytical solution were also observed in [53]. We also note that in the current work, we employ a variable soft sphere (VSS) model, while the work in [53] assumed a variable hard sphere (VHS) model. As shown in [28], the difference between centerline velocity in a 2D flow and a 3D flow can be around 40%. This indicates that the 2D work serves as verification work only, and it is difficult to extend the analytical solution to 3D.

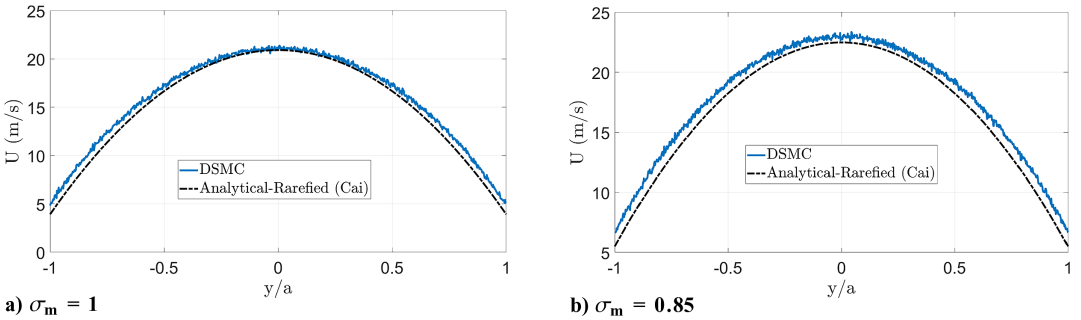

a) σ_m = 1 **b) σ_m = 0.85**

Fig. B1 Velocity profiles inside the pore at $x = 0.5L$ in the 2D channel compared to the analytical solution [53].

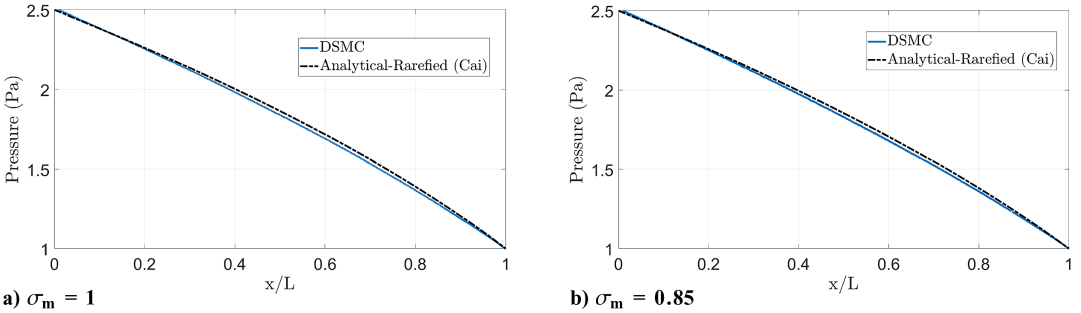

a) σ_m = 1 **b) σ_m = 0.85**

Fig. B2 Comparison of centerline pressure distribution in the 2D channel compared to the analytical solution [53].

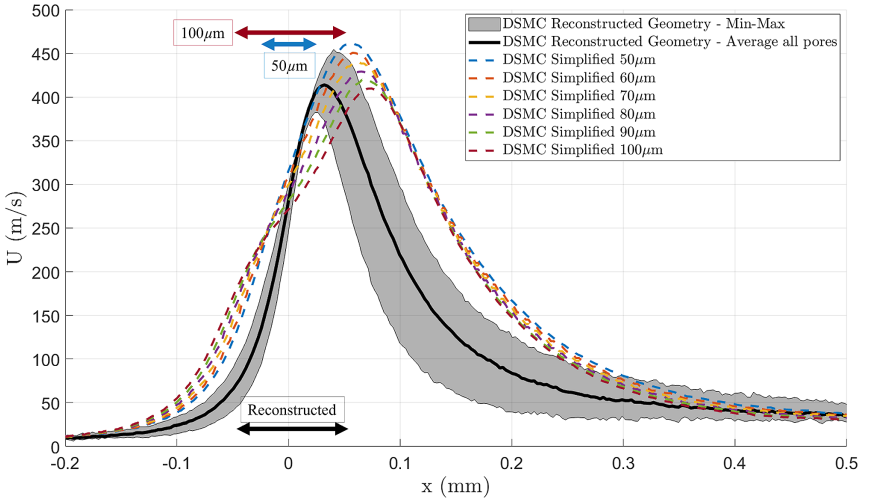

Fig. C1 Case 2 centerline velocity comparison between the reconstructed and simplified geometry for different pore thicknesses. Arrows indicate the thickness and locations of the different geometries.

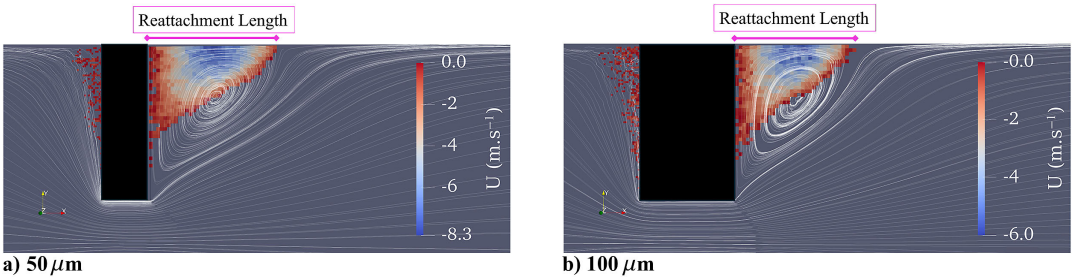

a) 50 μm **b) 100 μm**

Fig. C2 Streamlines showing the recirculation zone for DSMC simplified geometry results for different pore thicknesses from case 2. Velocity contours indicate flow in the negative *x* direction.

Appendix C: Low-*Re* Low-Density DSMC-Simplified Geometry Thickness Study

Multiple simulations with a simplified square pore geometry are performed where the thickness is in the range of 50–100 μm. As shown in Fig. C1, the centerline velocity increases as the thickness of the pore decreases, though discrepancies in the streamwise velocity profile upstream of the pore are still observed compared to the reconstructed geometry results.

Figure C2 highlights the recirculation behind the simplified pore geometry from DSMC results for Case 2 for two different pore thicknesses. This figure also shows how changing the thickness of the simplified geometry affects the reattachment length of the flow. We define the reattachment length to be the distance from the back of the pore to the point where the flow is once again in the positive streamwise direction, and Table C1 shows a minor increase in normalized reattachment length as the pore thickness is decreased.

Table C1 Reattachment length for different pore thicknesses in the DSMC-Simplified geometry simulations for Case 2

Thickness, μm	Reattachment length, μm	Normalized by the pore height
50	130.12	1.445
60	128.89	1.432
70	127.65	1.418
80	126.42	1.404
90	125.18	1.391
100	123.94	1.377

Acknowledgments

Parts of this work were performed at the Jet Propulsion Laboratory, California Institute of Technology, under a contract with NASA. Reference herein to any specific commercial product, process, or service by trade name, trademark, manufacturer, or otherwise does not constitute or imply its endorsement by the United States Government or the Jet Propulsion Laboratory, California Institute of Technology. Simulations in this work used the Anvil cluster at Purdue University through allocation MCH230049 from the Advanced Cyberinfrastructure Coordination Ecosystem: Services & Support (ACCESS) program, which is supported by National Science Foundation grants #2138259, #2138286, #2138307, #2137603, and #2138296, along with computational resources provided by the NASA High-End Computing (HEC) Program through the NASA Advanced Supercomputing (NAS) Division at Ames Research Center. Seyed Danial Ghasimi acknowledges partial support from the Jet Propulsion Laboratory, California Institute of Technology, through Subcontract No. 1691016. Savio Poovathingal and Luis Chacon were supported by a Space Technology Research Institutes grant from NASA's Space Technology Research Grants Program under grant number 80NSSC21K1117. The authors thank Arnaud Borner and Olivier Desjardins for valuable discussions related to the DSMC and CFD simulations, respectively, performed in this work. The authors would also like to thank the two anonymous peer reviewers for all of their comments and suggestions.

References

[1] Prakash, R., Burkhart, P. D., Chen, A., Comeaux, K. A., Guernsey, C. S., Kipp, D. M., Lorenzoni, L. V., Mendeck, G. F., Powell, R. W., Rivellini, T. P., et al., "Mars Science Laboratory Entry, Descent, and Landing System Overview," *2008 IEEE Aerospace Conference*, Inst.

of Electrical and Electronics Engineers, New York, 2008, pp. 1–18. https://doi.org/10.1109/AERO.2008.4526283

[2] Dutta, S., Karlgaard, C. D., Kass, D., Villar, G., and Mischna, M., "Post-Flight Analysis of Atmospheric Properties from Mars 2020 Entry, Descent, and Landing," *AIAA SCITECH 2022 Forum*, AIAA Paper 2022-0422, 2022. https://doi.org/10.2514/6.2022-0422

[3] Nelessen, A., Sackier, C., Clark, I., Brugarolas, P., Villar, G., Chen, A., Stehura, A., Otero, R., Stilley, E., Way, D., et al., "Mars 2020 Entry, Descent, and Landing System Overview," *2019 IEEE Aerospace Conference*, Inst. of Electrical and Electronics Engineers, New York, 2019, pp. 1–20. https://doi.org/10.1109/AERO.2019.8742167

[4] O'Farrell, C., Sonneveldt, B. S., Karhgaard, C., Tynis, J. A., and Clark, I. G., "Overview of the ASPIRE Project's Supersonic Flight Tests of a Strengthened DGB Parachute," *2019 IEEE Aerospace Conference*, Inst. of Electrical and Electronics Engineers, New York, 2019, pp. 1–18. https://doi.org/10.1109/AERO.2019.8741611

[5] Tanner, C. L., Clark, I. G., and Chen, A., "Overview of the Mars 2020 Parachute Risk Reduction Activity," *2018 IEEE Aerospace Conference*, Inst. of Electrical and Electronics Engineers, New York, 2018, pp. 1–11. https://doi.org/10.1109/AERO.2018.8396717

[6] Rabinovitch, J., Griffin, G. S., Seto, W., O'Farrell, C., Tanner, C. L., and Clark, I. G., "ASPIRE Supersonic Parachute Shape Reconstruction," *AIAA Scitech 2019 Forum*, AIAA Paper 2019-1629, 2019. https://doi.org/10.2514/6.2019-1629

[7] Dutta, S., "ASPIRE Parachute Modeling and Comparison to Post-Flight Reconstruction," *AIAA Scitech 2020 Forum*, AIAA Paper 2020-0756, 2020. https://doi.org/10.2514/6.2020-0756

[8] Karagiozis, K., Kamakoti, R., Cirak, F., and Pantano, C., "A Computational Study of Supersonic Disk-Gap-Band Parachutes Using Large-Eddy Simulation Coupled to a Structural Membrane," *Journal of Fluids and Structures*, Vol. 27, No. 2, 2011, pp. 175–192. https://doi.org/10.1016/j.jfluidstructs.2010.11.007

[9] Huang, D. Z., Avery, P., Farhat, C., Rabinovitch, J., Derkevorkian, A., and Peterson, L. D., "Modeling, Simulation and Validation of Supersonic Parachute Inflation Dynamics During Mars Landing," *AIAA Scitech 2020 Forum*, AIAA Paper 2020-0313, 2020. https://doi.org/10.2514/6.2020-0313

[10] Cadieux, F., Angel, J. B., Barad, M. F., and Kiris, C. C., "Fluid-Structure Interaction Simulations of the ASPIRE SR03 Supersonic Parachute Flight Test," *AIAA SCITECH 2023 Forum*, AIAA Paper 2023-1336, 2023. https://doi.org/10.2514/6.2023-1336

[11] Yu, H., Pantano, C., and Cirak, F., "Large-Eddy Simulation of Flow Over Deformable Parachutes Using Immersed Boundary and Adaptive Mesh," *AIAA Scitech 2019 Forum*, AIAA Paper 2019-0635, 2019. https://doi.org/10.2514/6.2019-0635

[12] As'ad, F., Avery, P., Farhat, C., Rabinovitch, J., Lobbia, M., and Ataei, N., "Sensitivity Analysis and Validation of a Computational Framework for Supersonic Parachute Inflation Dynamics," *AIAA Journal*, Vol. 63, No. 5, 2024, pp. 1743–1763. https://doi.org/10.2514/1.J064791

[13] Cruz, J. R., O'Farrell, C., Hennings, E., and Runnells, P., "Permeability of Two Parachute Fabrics—Measurements, Modeling, and Application," *24th AIAA Aerodynamic Decelerator Systems Technology Conference*, AIAA Paper 2017-3725, 2017. https://doi.org/10.2514/6.2017-3725

[14] Cruz, J. R., Hennings, E., and Runnells, P., "Permeability of a New Parachute Fabric—Measurements, Modeling, and Application," NASA TM 2018-220112, Hampton, VA, 2018, https://ntrs.nasa.gov/citations/20190001214.

[15] Siegel, K. J., O'Farrell, C., and Lowry, C. W., "Parachute Broadcloth Development for Use on Mars Sample Retrieval Lander," *26th AIAA Aerodynamic Decelerator Systems Technology Conference*, AIAA Paper 2022-2740, 2022. https://doi.org/10.2514/6.2022-2740

[16] Phillippe, C. A., Panerai, F., and Roca, L. V., "In Situ Imaging of Parachute Textile Micromechanics Under Tensile Load," *AIAA Journal*, Vol. 62, No. 12, 2024, pp. 4691–4700. https://doi.org/10.2514/1.J064350

[17] Phillippe, C., Ehrhardt, D., Panerai, F., and Roca, L. V., "Flow-Induced Strain of Parachute Textiles With Multiscale Digital Image Correlation," *AIAA SCITECH 2025 Forum*, AIAA Paper 2025-2640, 2025. https://doi.org/10.2514/6.2025-2640

[18] Payne, P. R., "The Theory of Fabric Porosity as Applied to Parachutes in Incompressible Flow," *Aeronautical Quarterly*, Vol. 29, No. 3, 1978, pp. 175–206. https://doi.org/10.1017/S000192590000843X

[19] Muskat, M., "The Flow of Compressible Fluids Through Porous Media and Some Problems in Heat Conduction," *Physics*, Vol. 5, No. 3, 1934, pp. 71–94. https://doi.org/10.1063/1.1745233

[20] Shepherd, J., and Begeal, D., "Transient Compressible Flow in Porous Materials," NASA TR 22324, Vol. 88, Jan. 1988, https://shepherd.caltech.edu/EDL/publications/reprints/SAND83-1788.pdf.

[21] Schmidt, B., "Compressible Flow Through Porous Media with Application to Injection," *Internal Report for Caltech Hypersonics Group*, California Inst. of Technology IR-FM-2014.001, Pasadena, CA, 2014, https://shepherd.caltech.edu/T5/publications/PorousMediaReport.pdf.

[22] Mendez, S., and Nicoud, F., "Adiabatic Homogeneous Model for Flow Around a Multiperforated Plate," *AIAA Journal*, Vol. 46, No. 10, 2008, pp. 2623–2633. https://doi.org/10.2514/1.37008

[23] Huang, D. Z., Wong, M. L., Lele, S. K., and Farhat, C., "Homogenized Flux-Body Force Treatment of Compressible Viscous Porous Wall Boundary Conditions," *AIAA Journal*, Vol. 59, No. 6, 2021, pp. 2045–2059. https://doi.org/10.2514/1.J059945

[24] Yu, H., and Pantano, C., "An Immersed Boundary Method with Implicit Body Force for Compressible Viscous Flow," *Journal of Computational Physics*, Vol. 459, June 2022, Paper 111125. https://doi.org/10.1016/j.jcp.2022.111125

[25] Boustani, J., Anugrah, G., Barad, M. F., Kiris, C. C., and Brehm, C., "A Numerical Investigation of Parachute Deployment in Supersonic Flow," *AIAA Scitech 2020 Forum*, AIAA Paper 2020-1050, 2020. https://doi.org/10.2514/6.2020-1050

[26] Boustani, J., Barad, M. F., Kiris, C. C., and Brehm, C., "An Immersed Interface Methodology for Simulating Supersonic Spacecraft Parachutes with Fluid–Structure Interaction," *Journal of Fluids and Structures*, Vol. 114, Oct. 2022, Paper 103742. https://doi.org/10.1016/j.jfluidstructs.2022.103742

[27] Ghasimi, S. D., and Rabinovitch, J., "Thin Surface Permeability Modeling for Mars Supersonic Parachute Inflations," *AIAA SCITECH 2023 Forum*, AIAA Paper 2023-0461, 2023. https://doi.org/10.2514/6.2023-0461

[28] Jain, V., and Lin, C. X., "Numerical Modeling of Three-Dimensional Compressible Gas Flow in Microchannnels," *Journal of Micromechanics and Microengineering*, Vol. 16, No. 2, 2006, pp. 292–302. https://doi.org/10.1088/0960-1317/16/2/014

[29] Alexeenko, A., Gimelshein, S., and Levin, D., "Reconsideration of Low Reynolds Number Flow-Through Constriction Microchannels Using the DSMC Method," *Journal of Microelectromechanical Systems*, Vol. 14, No. 4, 2005, pp. 847–856. https://doi.org/10.1109/JMEMS.2005.846040

[30] Arkilic, E., Schmidt, M., and Breuer, K., "Gaseous Slip Flow in Long Microchannels," *Journal of Microelectromechanical Systems*, Vol. 6, No. 2, 1997, pp. 167–178. https://doi.org/10.1109/84.585795

[31] Dongari, N., Agrawal, A., and Agrawal, A., "Analytical Solution of Gaseous Slip Flow in Long Microchannels," *International Journal of Heat and Mass Transfer*, Vol. 50, No. 17, 2007, pp. 3411–3421. https://doi.org/10.1016/j.ijheatmasstransfer.2007.01.048

[32] Guo, X., Huang, C., Alexeenko, A., and Sullivan, J., "Numerical and Experimental Study of Gas Flows in 2D and 3D Microchannels," *Journal of Micromechanics and Microengineering*, Vol. 18, No. 2, 2008, Paper 025034. https://doi.org/10.1088/0960-1317/18/2/025034

[33] Bird, G. A., *Molecular Gas Dynamics and the Direct Simulation of Gas Flows*, Oxford Univ. Press, Oxford, 1994, https://ui.adsabs.harvard.edu/abs/1994mgdd.book.B.

[34] Desjardins, O., "NGA 2 Github," 2024, https://github.com/desjardi/NGA2.

[35] Desjardins, O., Blanquart, G., Balarac, G., and Pitsch, H., "High Order Conservative Finite Difference Scheme for Variable Density Low Mach Number Turbulent Flows," *Journal of Computational Physics*, Vol. 227, No. 15, 2008, pp. 7125–7159. https://doi.org/10.1016/j.jcp.2008.03.027

[36] Kuhn, M. B., and Desjardins, O., "An All-Mach, Low-Dissipation Strategy for Simulating Multiphase Flows," *Journal of Computational Physics*, Vol. 445, Nov. 2021, Paper 110602. https://doi.org/10.1016/j.jcp.2021.110602

[37] Geuzaine, P., Brown, G., Harris, C., and Farhat, C., "Aeroelastic Dynamic Analysis of a Full F-16 Configuration for Various Flight Conditions," *AIAA Journal*, Vol. 41, No. 3, 2003, pp. 363–371. https://doi.org/10.2514/2.1975

[38] Farhat, C., Geuzaine, P., and Brown, G., "Application of a Three-Field Nonlinear Fluid–Structure Formulation to the Prediction of the Aeroelastic Parameters of an F-16 Fighter," *Computers and Fluids*, Vol. 32, No. 1, 2003, pp. 3–29. https://doi.org/10.1016/S0045-7930(01)00104-9

[39] Main, A., Zeng, X., Avery, P., and Farhat, C., "An Enhanced FIVER Method for Multi-Material Flow Problems with Second-Order Convergence Rate," *Journal of Computational Physics*, Vol. 329, Jan. 2017, pp. 141–172. https://doi.org/10.1016/j.jcp.2016.10.028

[40] Farhat Research Group (FRG), "AERO Suite," 2024, https://bitbucket.org/frg/.

[41] Plimpton, S. J., Moore, S. G., Borner, A., Stagg, A. K., Koehler, T. P., Torczynski, J. R., and Gallis, M. A., "Direct Simulation Monte Carlo on Petaflop Supercomputers and Beyond," *Physics of Fluids*, Vol. 31, No. 8, 2019, Paper 086101. https://doi.org/10.1063/1.5108534

[42] Sandia National Laboratory, "SPARTA," 2024, https://sparta.github.io/.

[43] Boerner, T. J., Deems, S., Furlani, T. R., Knuth, S. L., and Towns, J., "ACCESS: Advancing Innovation: NSF's Advanced Cyberinfrastructure Coordination Ecosystem: Services & Support," *Practice and Experience in Advanced Research Computing*, Assoc. for Computing Machinery, New York, 2023, pp. 173–176. https://doi.org/10.1145/3569951.3597559

[44] Franquet, E., Perrier, V., Gibout, S., and Bruel, P., "Free Underexpanded Jets in a Quiescent Medium: A Review," *Progress in Aerospace Sciences*, Vol. 77, Aug. 2015, pp. 25–53. https://doi.org/10.1016/j.paerosci.2015.06.006

[45] White, F. M., *Viscous Fluid Flow*, McGraw Hill Series in Mechanical Engineering, McGraw-Hill, New York, 2006, pp. 107, 113.

[46] Kundu, P. K., Cohen, I. M., Dowling, D. R., and Capecelatro, J., *Fluid Mechanics*, Elsevier, New York, 2024, pp. 98–101.

[47] Ahmad, T., and Hassan, I., "Experimental Analysis of Microchannel Entrance Length Characteristics Using Microparticle Image Velocimetry," *Journal of Fluids Engineering*, Vol. 132, No. 4, 2010, Paper 041102. https://doi.org/10.1115/1.4001292

[48] Durst, F., Ray, S., Ünsal, B., and Bayoumi, O. A., "The Development Lengths of Laminar Pipe and Channel Flows," *Journal of Fluids Engineering*, Vol. 127, No. 6, 2005, pp. 1154–1160. https://doi.org/10.1115/1.2063088

[49] Higdon, K. J., "Monte Carlo Sensitivity Analyses of DSMC Parameters for Ionizing Hypersonic Flows," Ph.D. Thesis, Univ. of Texas at Austin, Austin, TX, 2018.

[50] Zhu, T., Li, Z., and Levin, D. A., "Modeling of Unsteady Shock Tube Flows Using Direct Simulation Monte Carlo," *Journal of Thermophysics and Heat Transfer*, Vol. 28, No. 4, 2014, pp. 623–634. https://doi.org/10.2514/1.T4419

[51] Toro, E. F., *Riemann Solvers and Numerical Methods for Fluid Dynamics: A Practical Introduction*, Springer-Verlag, Berlin, 2009, pp. 212–225. https://doi.org/10.1007/b79761

[52] Rabinovitch, J., Griffin, G. S., Seto, W., O'Farrell, C., Tanner, C. L., and Clark, I. G., "Full-Scale Supersonic Parachute Shape Reconstruction Using Three-Dimensional Stereo Imagery," *Journal of Spacecraft and Rockets*, Vol. 57, No. 6, 2020, pp. 1139–1152. https://doi.org/10.2514/1.A34717

[53] Cai, C., Boyd, I. D., Fan, J., and Candler, G. V., "Direct Simulation Methods for Low-Speed Microchannel Flows," *Journal of Thermophysics and Heat Transfer*, Vol. 14, No. 3, 2000, pp. 368–378. https://doi.org/10.2514/2.6534

S. Shin
Associate Editor